LAWRENCE
LIVERMORE
NATIONAL
LABORATORY

Cosmos++: Relativistic Magnetohydrodynamics on Unstructured Grids with Local Adaptive Refinement

P. Anninos, P. C. Fragile, J. D. Salmonson

May 10, 2005

Disclaimer

Cosmos++ : Relativistic Magnetohydrodynamics on Unstructured Grids with Local Adaptive Refinement

Peter Anninos[1], P. Chris Fragile[2], and Jay D. Salmonson[1]

ABSTRACT

A new code and methodology are introduced for solving the fully general relativistic magnetohydrodynamic (GRMHD) equations using time-explicit, finite-volume discretization. The code has options for solving the GRMHD equations using traditional artificial-viscosity (AV) or non-oscillatory central difference (NOCD) methods, or a new extended AV (eAV) scheme using artificial-viscosity together with a dual energy-flux-conserving formulation. The dual energy approach allows for accurate modeling of highly relativistic flows at boost factors well beyond what has been achieved to date by standard artificial viscosity methods. It provides the benefit of Godunov methods in capturing high Lorentz boosted flows but without complicated Riemann solvers, and the advantages of traditional artificial viscosity methods in their speed and flexibility. Additionally, the GRMHD equations are solved on an unstructured grid that supports local adaptive mesh refinement using a fully threaded oct-tree (in three dimensions) network to traverse the grid hierarchy across levels and immediate neighbors. A number of tests are presented to demonstrate robustness of the numerical algorithms and adaptive mesh framework over a wide spectrum of problems, boosts, and astrophysical applications, including relativistic shock tubes, shock collisions, magnetosonic shocks, Alfvén wave propagation, blast waves, magnetized Bondi flow, and the magneto-rotational instability in Kerr black hole spacetimes.

Subject headings: hydrodynamics — methods: numerical — MHD — relativity

1. Introduction

Magnetohydrodynamic (MHD) driven processes in high-energy astrophysical environments can be extremely difficult to model numerically, especially where flows are strongly trans-sonic, characteristic speeds approach the speed of light, or nonlinear effects couple over short temporal and large spatial dynamical ranges. For example, studies of phase transitions in the early universe (Fragile & Anninos 2003), and the formation of primordial magnetic fields and black holes demand resolution across many decades of scale to model phase interactions, wall dynamics, and microphysical coupling effects. Similarly, simulations of black hole accretion flows (e.g. Fragile & Anninos 2005), thought to exist in quasars, active galactic nuclei, X-ray binaries, core-collapse supernovae, and gamma-ray bursts, require stably evolving the GRMHD equations in a strongly curved background spacetime over many dynamical scales. Addressing such problems requires numerical algorithms that are robust enough to simulate ultra-relativistic waves and shocks, and accurate enough to treat various physical instabilities that can be seeded at very small amplitudes and frequencies

---

[1] University of California, Lawrence Livermore National Laboratory, Livermore CA 94550

[2] Department of Physics, University of California, Santa Barbara, CA 93106; fragile@physics.ucsb.edu

and yet affect global solutions. We also desire algorithms that can capture the propagation of outflows or highly compressed features beyond the limits imposed by single mesh simulations.

A number of codes have been developed in recent years to solve both the special and general relativistic MHD equations. Our approach is most similar to that taken by De Villiers & Hawley (2003a), which is based on an internal energy formulation with artificial viscosity (AV) for shock capturing and a method of characteristics for the magnetic fields. However, other approaches include the simplified total variation diminishing (sTVD) method (Koide et al. 1999) and high order Godunov schemes (Gammie et al. 2003; Komissarov 1999) based on fully conservative formulations of the MHD equations. Godunov methods are significantly more complex than either the AV or sTVD schemes due to the Riemann solvers, but are considered more robust for ultra-relativistic problems. Although viscosity-based methods are generally accurate, fast, simple to implement, and easy to expand to include multi-physics capabilities, they have historically been limited in their range of applicability to moderately relativistic flows, with boost factors less than a few.

In this paper we describe a new massively parallel, multi-dimensional numerical code *Cosmos++* with improved (over traditional AV methods) shock capturing capabilities in the high boost regime and adaptive mesh refinement (AMR), representing a significant advance over our previous numerical code (*Cosmos* , Anninos & Fragile 2003). *Cosmos++* introduces a more complex unstructured mesh system that allows for arbitrarily connected hexahedral (quadrilateral in 2D) cells to conform to any boundary or shape. It also allows for dentritic-type zoning characteristic of refined grids at level interfaces. Our AMR framework differs from the more standard approach (Berger & Oliger 1984; Berger & Colella 1989) by refining individual cells rather than introducing patches of sub-grids composed of multi-dimensional arrays of cells, thus providing greater flexibility in modeling complex flows and greater efficiency in positioning computational resources. This framework is similar to that described by Khokhlov (1998), but we generalize the method to unstructured meshes. Also, as in our predecessor code, several schemes have been implemented to solve the hydrodynamical equations, including both artificial viscosity and non-oscillatory central difference (NOCD) methods. However, here we use discrete finite-volume methods in place of finite differences due to the unstructured nature of the grid. We also introduce in this paper a new dual energy procedure (eAV) that allows conventional artificial viscosity methods to be extended and work robustly at arbitrarily high Lorentz factors.

The basic equations, numerical methods, and tests of the code are described in the remaining sections. Although *Cosmos++* supports many different physics packages in both covariant Newtonian and general relativistic systems, including chemical networks, flux-limited radiation diffusion, self-gravity, magnetic fields, and radiative cooling, only the GRMHD algorithms in the AMR framework are covered in this paper. The Newtonian physics capabilities are currently the same as those of *Cosmos* , which were presented in Anninos et al. (2003) and Fragile et al. (2005).

2. Basic Equations

Two separate formulations of the GRMHD equations are presented in this section. The first form incorporates an evolution equation for the internal energy that is appropriate for schemes using artificial viscosity methods for capturing shocks (Wilson 1972, 1979; Hawley et al. 1984). The second form is derived directly from the primitive form of stress-energy conservation and is thus fully conservative and provides the basis for the non-oscillatory central difference schemes. We use the standard notation in which 4(3)-dimensional tensor quantities are represented by Greek(Latin) indices.

For a perfect fluid, the stress-energy tensor is generated from a linear sum of the hydrodynamic $T_H^{\mu\nu}$ and magnetic contributions $T_B^{\mu\nu}$

$$
\begin{aligned}
T^{\mu\nu} &= T_H^{\mu\nu} + T_B^{\mu\nu} \\
&= \rho h u^\mu u^\nu + P g^{\mu\nu} + \frac{1}{4\pi}\left(\frac{1}{2}g^{\mu\nu}||B||^2 + u^\mu u^\nu ||B||^2 - B^\mu B^\nu\right) \\
&= \left(\rho h + 2P_B\right) u^\mu u^\nu + \left(P + P_B\right) g^{\mu\nu} - \frac{1}{4\pi} B^\mu B^\nu ,
\end{aligned}
\tag{1}
$$

where

$$
h = 1 + \epsilon + \frac{P}{\rho} + \frac{||Q||}{\rho} = 1 + \Gamma\epsilon + \frac{||Q||}{\rho}
\tag{2}
$$

is the relativistic enthalpy, ϵ is the specific internal energy, P is the fluid pressure, $||Q||$ is the bulk scalar (artificial) viscosity, $P_B = ||B||^2/8\pi = g_{\mu\nu}B^\mu B^\nu/8\pi$ is the magnetic pressure, and B^μ is the magnetic induction in the rest frame of the fluid. Also, u^μ is the contravariant 4-velocity, $g_{\mu\nu}$ is the 4-metric, and Γ is the adiabatic index assuming an ideal gas equation of state $P = (\Gamma - 1)\rho\epsilon$.

2.1. Internal Energy Formulation

This method uses a form of the GRMHD equations similar to De Villiers & Hawley (2003a), derived from velocity normalization $u_\mu u^\mu = -1$, baryon conservation $\nabla_\mu(\rho u^\mu) = 0$, energy conservation $u_\nu \nabla_\mu T^{\mu\nu} = 0$, momentum conservation $(g_{\alpha\nu} + u_\alpha u_\nu)\nabla_\mu T^{\mu\nu} = 0$, and magnetic induction $\nabla_\mu(u^\mu B^\nu - B^\mu u^\nu) = 0$. Nevertheless, it is worth explicitly writing these equations out for clarity, since we employ a unique expansion and grouping of the terms in our numerical implementation. In flux-conserving form, the evolution equations for mass, internal energy, momentum, and magnetic induction are:

$$
\partial_t D + \partial_i(DV^i) = 0 ,
\tag{3}
$$

$$
\partial_t E + \partial_i(EV^i) = -\left(P + k_{\dot{W}}||Q||\right)\partial_t W - \left(P\delta_i^j + Q_i^j\right)\partial_j(WV^i) ,
\tag{4}
$$

$$
\begin{aligned}
\partial_t S_j + \partial_i(S_j V^i) = & \frac{1}{4\pi}\partial_t(\sqrt{-g}B_j B^0) + \frac{1}{4\pi}\partial_i(\sqrt{-g}B_j B^i) \\
& + \left(\frac{S^\mu S^\nu}{2S^0} - \frac{\sqrt{-g}}{8\pi}B^\mu B^\nu\right)\partial_j g_{\mu\nu} - \sqrt{-g}\,\partial_i((P+P_B)\delta_j^i + Q_j^i) ,
\end{aligned}
\tag{5}
$$

$$
\partial_t \mathcal{B}^j + \partial_i(\mathcal{B}^j V^i) = \mathcal{B}^i \partial_i V^j + \eta\,\partial^j(\partial_i \mathcal{B}^i) ,
\tag{6}
$$

where g is the 4-metric determinant, δ_j^i is the Kronecker delta tensor, $W = \sqrt{-g}u^0$ is the relativistic boost factor, $D = W\rho$ is the generalized fluid density, $V^i = u^i/u^0$ is the transport velocity, $S_\mu = W(\rho h + 2P_B)u_\mu$ is the covariant momentum density, $E = We = W\rho\epsilon$ is the generalized internal energy density, Q_j^i is the tensor artificial viscosity used for shock capturing, $k_{\dot{W}}$ is a switch used to activate a viscosity multiplier for the $\partial_t W$ source, and η is a coefficient related to the largest characteristic speed in the flow multiplying the divergence cleanser function. Notice there are two representations of the magnetic field in these equations: B^μ is the rest frame magnetic field 4-vector defined in the stress tensor definition (1) and

$$
\mathcal{B}^\mu = W(B^\mu - B^0 V^\mu)
\tag{7}
$$

is the divergence-free ($\partial \mathcal{B}^i/\partial x^i = 0$), spatial ($\mathcal{B}^0 = 0$) representation of the field. The time component of the magnetic field B^0 is recovered from the orthogonality condition $B^\mu u_\mu = 0$

$$B^0 = -\frac{g_{0i}B^i + g_{ij}B^jV^i}{g_{00} + g_{0i}V^i} = -\frac{g_{0i}\mathcal{B}^i + g_{ij}\mathcal{B}^jV^i}{W(g_{00} + 2g_{0i}V^i + g_{ij}V^iV^j)} \tag{8}$$

$$= \frac{\mathcal{B}^iS_i}{\sqrt{-g}W(\rho h + 2P_B)} , \tag{9}$$

and we use

$$P_B = \frac{1}{8\pi}g_{\mu\nu}B^\mu B^\nu = \frac{1}{8\pi}\frac{g_{ij}\mathcal{B}^i\mathcal{B}^j}{W^2} + \frac{1}{8\pi}\left(\frac{B^0\sqrt{-g}}{W}\right)^2 \tag{10}$$

to compute the magnetic pressure from the divergence-free field.

We note that the term $\partial_i(\sqrt{-g}B_jB^i)$ in equation (5) can be cast into projected and divergence components $B^i\partial_i(\sqrt{-g}B_j) + \sqrt{-g}B_j\partial_iB^i$. The advantage of this form is that the method of characteristics described by Stone et al. (1992) can be applied easily to the projected component after generalizing the definitions of density and momentum accounting for relativistic inertia and boost contributions. This procedure is important for achieving stable simulations of sheared Alfvén waves, as demonstrated in §4.2.1.

Two additional sets of equations are needed for the transport velocity V^i and boost factor W. The velocity is derived from the 4-momentum normalization $S_\mu S^\mu = W^2(\rho h + 2P_B)^2 u_\mu u^\mu = -W^2(\rho h + 2P_B)^2$, from which we compute

$$S_0 = -\frac{g^{0i}S_i}{g^{00}} + \frac{1}{g^{00}}\left[\left(g^{0i}S_i\right)^2 - g^{00}\left(W^2(\rho h + 2P_B)^2 + g^{ij}S_iS_j\right)\right]^{1/2} , \tag{11}$$

and then $V^i = S^i/S^0$. A convenient formula is derived for the boost factor using u^0 obtained from the 4-velocity normalization written as $u_\mu u^\mu = u^0 V^\mu S_\mu/(W(\rho h + 2P_B)) = -1$. The boost ($W = \sqrt{-g}u^0$) is then evaluated in one of two ways

$$W = -\frac{\sqrt{-g}(-S_\mu S^\mu)^{1/2}}{S_\mu V^\mu} = \frac{\sqrt{-g}S^0}{(-S_\mu S^\mu)^{1/2}} , \tag{12}$$

where $V^0 = 1$, S^0 is computed from the 4-momentum normalization described above, and the other fields are known from solutions to the evolution equations.

2.2. Conservative Energy Formulation

A second class of numerical methods presented in this paper are based on a conservative hyperbolic formulation of the GRMHD equations. It is the same approach used by Anninos & Fragile (2003), except here we include magnetic fields. The equations are derived directly from the conservation of stress-energy $\nabla_\mu T^{\mu\nu} = 0$ and then decomposed into space and time components

$$\partial_t(\sqrt{-g}\,T^{0\nu}) + \partial_i(\sqrt{-g}\,T^{i\nu}) = \Sigma^\nu, \tag{13}$$

with curvature source terms

$$\Sigma^\nu = -\sqrt{-g}\,T^{\beta\gamma}\,\Gamma^\nu_{\beta\gamma}. \tag{14}$$

The form of the differential equations that we solve, derived after substituting the perfect fluid stress tensor (1) into (13), are

$$\partial_t \mathcal{E} + \partial_i (\mathcal{E} V^i) + \partial_i F^{0i} \;=\; \Sigma^0 \;, \tag{15}$$

$$\partial_t \mathcal{S}^j + \partial_i (\mathcal{S}^j V^i) + \partial_i F^{ij} \;=\; \Sigma^j \;, \tag{16}$$

where we have explicitly split off the transport term from the other divergence flux contributions $F^{i\alpha}$, defined as

$$F^{i\alpha} = \sqrt{-g} \left((g^{i\alpha} - g^{0\alpha} V^i)\,(P + P_B) - \frac{1}{4\pi}(B^i B^\alpha - B^0 B^\alpha V^i) \right) \;. \tag{17}$$

The variables D, V^i, and g are defined as in section §2.1, and

$$\mathcal{E} = \sqrt{-g} T^{00} \;=\; \frac{W^2}{\sqrt{-g}}(\rho h + 2 P_B) + \sqrt{-g}\, g^{00}(P + P_B) - \frac{1}{4\pi}\sqrt{-g} B^0 B^0 \;, \tag{18}$$

$$\mathcal{S}^j = \sqrt{-g} T^{0j} \;=\; \frac{W^2}{\sqrt{-g}}(\rho h + 2 P_B) V^j + \sqrt{-g}\, g^{0j}(P + P_B) - \frac{1}{4\pi}\sqrt{-g} B^0 B^j \;, \tag{19}$$

$$\tag{20}$$

are the new expressions for energy and momentum. We also note that the divergence-free magnetic induction equation (6) can be written in the fully conservative form

$$\partial_t \mathcal{B}^j + \partial_i (\mathcal{B}^j V^i - \mathcal{B}^i V^j) = \eta\, \partial^j (\partial_i \mathcal{B}^i) \;, \tag{21}$$

as required by the central difference schemes described in §3.2.

It is convenient to express $\mathcal{E}$ and $\mathcal{S}^i$ in terms of the internal energy fields E and S_α

$$\mathcal{E} \;=\; \frac{W^2}{\sqrt{-g}}\left(\frac{D}{W} + \Gamma\frac{E}{W} + 2 P_B\right) + \sqrt{-g}\, g^{00}\left((\Gamma - 1)\frac{E}{W} + P_B\right) - \frac{1}{4\pi}\sqrt{-g} B^0 B^0 \;, \tag{22}$$

$$\mathcal{S}^j \;=\; g^{j\alpha} S_\alpha + \sqrt{-g}\, g^{0j}\left((\Gamma - 1)\frac{E}{W} + P_B\right) - \frac{1}{4\pi}\sqrt{-g} B^0 B^j \;. \tag{23}$$

The inverse energy relation

$$\frac{E}{W} = \left(\frac{\mathcal{E}\sqrt{-g}}{W^2} - \frac{D}{W} - 2 P_B - \left(\frac{\sqrt{-g}}{W}\right)^2 \left(g^{00} P_B - \frac{B^0 B^0}{4\pi}\right) \right) \frac{1}{\Gamma + (\Gamma - 1)g^{00}(\sqrt{-g}/W)^2} \tag{24}$$

is useful for computing the fluid pressure ($P = (\Gamma - 1)E/W$), and for comparing relative errors in the dual energy update procedure described in §3.

3. Numerical Methods

Cosmos++ is designed using object-oriented principles to create abstraction classes for vector and tensor (both three and four dimensional) functions on which most mathematical operations are based. *Cosmos++* also takes advantage of the operator overload, inheritance, polymorphism and virtual methods features of the *C++* language in its design of the zone, mesh, refinement, physics, boundary condition, data exchange, and output classes. This simplifies the user interface considerably, reduces the amount of coding, and allows for the code to be easily developed and expanded. All data structures (mesh and fields) are stored as vector or

map container classes using the $C++$ Standard Template Library (STL) which provides convenient memory access functions and other useful support features (e.g., sorting, searching) for interacting with the data. Multi-dimensional STL vectors are used as storage containers for pointers to zone objects at each refinement level, which include all the field, cell and connectivity data as class member attributes. STL maps provide an efficient mechanism to identify direct and inverse relations between zone iterators and unique global zone identifications.

The essential cell geometry used in constructing meshes for $Cosmos++$ is a quadrilateral (hexahedral) shape in two (three) spatial dimensions. In order to provide enough flexibility so individual cells can be arranged in an arbitrarily distorted and unstructured fashion, allowing even reduced or enhanced nodal connectivities, we store a number of attributes for each cell, including node positions, inward (towards the cell center) pointing face area normals, and zone volumes for convenience. Each zone also carries pointers to all of its neighbors sharing a common cell face. Where a neighbor cell has been refined to a higher level, the pointer references the neighbor's parent so that neighbors are always at or below the refinement level of the referencing cell and there is at most one neighbor for each cell face. The actual operational neighbors are found by selecting the neighbor's appropriate children if they exist. Neighbor searches are carried out each time a refinement cycle adjusts the mesh, and performed with local tree scans by going up to the parent, across to the neighbors, then down through the child zone lists. This is done to allow greater flexibility and simplicity during the refinement cycle in case, for example, a cell and its neighbors are tagged for de-refinement simultaneously. When a cell is refined, it is decomposed into two, four or eight sub-cells in one, two or three dimensions, and pointers to these newly allocated child zones are stored in ordered contiguous fashion for fast and easy reference. Each child zone, in turn, carries a pointer to its parent cell. As a result, all cells in the mesh are fully threaded with local binary-, quad-, or oct-tree parent-child hierarchies and semi-direct neighbor access.

$Cosmos++$ currently supports several refinement criteria, including field value, normalized field gradient, normalized field curvature, mass, and Jeans mass. When either of the field, gradient, or curvature options are selected, the user can specify any stored variable upon which to apply the criterion. Also, as an option, the refinement criterion can be computed for either the evolved fields or their conformal counterparts (by dividing out the metric determinant), which is useful to track only flow (not metric) features. Fields in newly created refined cells are reconstructed by a linear, conservative, and monotonic interpolation of nearest neighbor and parent data.

Numerical calculations are performed in the physics packages only across the list of leaf zones which have no children. The effective mesh is thus unstructured in general, composed of many different sized zones containing any number of hanging nodes with reduced nodal connectivity. In order to accomodate these kinds of meshes (and even more general ones) we use finite volume, in place of finite difference, methods to solve the GRMHD differential equations. Simple derivatives are computed using standard second order (on uniform meshes) finite volume discretization. Gradients of a generic vector field T_i, for example, are evaluated by averaging the gradient function over a single cell control volume and converting the volume integral into a surface summation

$$G_{ij} \equiv \partial_j T_i = \frac{1}{V_z} \int_{\mathrm{d}V} \partial_j T_i \, \mathrm{d}V = -\frac{1}{V_z} \oint T_i \, \mathrm{d}A_j = -\frac{1}{V_z} \sum_f^{\mathrm{faces}} (T_i^* \, A_j)_f \; , \tag{25}$$

where the summation is performed over all cell faces. Here V_z is the zone volume, A_j is the area vector normal to the cell face (f) pointing inwards toward the cell center, T_i^* is the appropriately averaged (or upwinded) field value at the cell faces, and the gradient is returned as a tensor with rows (columns) representing the

vector (gradient) directions (in usual gradient index notation $G_{ij} = T_{i,j}$). The negative sign in (25) is a result of choosing an inward pointing area vector. Many of the gradient calculations appearing as source terms in a typical time sequence update are computed using a variation of the above expression. Some of the other, more specialized, operations used in solving the GRMHD equations in the different formalisms are described below.

3.1. AV Method

3.1.1. Advection

Advection is solved for each evolved field quantity using a first (second) order in time (space) procedure and the scalar divergence form of equation (25). Letting $\mathbf{F}$ represent any of the evolved fields (D, E, S_j, B^j), the discrete, finite-volume representation of the transport source follows from (25)

$$\partial_i(\mathbf{F}V^i) = -\frac{1}{V_z} \sum_f^{faces} (\mathbf{F}^* \, V^i \, A_i)_f \; , \tag{26}$$

where V_z is the local donor zone volume, $(A_i)_f$ is the inward pointing area normal vector of face f, and $(V^i)_f$ is the face-centered velocity defined as a weighted average across neighboring cells. The quantity $(\mathbf{F}^*)_f$ represents first order zone-centered fields estimated at each cell face by a Taylor's expansion using limited gradient extrapolants, $\mathbf{F}^* = \mathbf{F}_z + (\partial_i\mathbf{F})_z^L(r^i - r_z^i)$, projected from the donor cell center r_z^i to either the face center $r^i = r_f^i$ or the advection control volume $r^i = r_f^i - (\Delta t/2)(V^i)_f$, over a time-step interval Δt.

The zone-centered limited gradient $(\partial_i\mathbf{F})_z^L$ is constrained to force monotonicity in the extrapolated fields. In the case of unstructured meshes, this is achieved by identifying three unique control volumes which we assign as upstream, downstream, or average. The average control volume is simply the total cell volume. Upstream and downstream volumes are constructed from the sub-zonal tetrahedral (triangular) in 3D (2D) geometric elements composed of node positions connecting a cell face center, one (two) zone nodes in 2D (3D), and the zone center. A sub-zone associated with the cell face f is defined as upstream (downstream) if the sign of the vector product $(A_iV^i)_f$ is positive (negative). The total upstream and downstream volumes are the sum of the tetrahedral (triangular) sub-zones matching the corresponding signature criteria. Gradient operators are then computed with (25) on each of these unique, arbitrary polyhedral (polygonal) sub-volumes, as surface integrals with appropriately averaged fields at each surface element boundary. We denote these gradients as $\partial_i^U\mathbf{F}$, $\partial_i^D\mathbf{F}$, and $\partial_i^A\mathbf{F}$ for the upstream, downstream, and average, respectively. To enforce monotonicity, the actual limited gradient $(\partial_i\mathbf{F})_z^L$ is set to zero if the vector product of any combination of the three gradient operators is negative. The gradient is limited further to various degrees of sharpness by defining the normalized scalar $\theta_\ell = \partial_\ell^U\mathbf{F}/(\partial_\ell^D\mathbf{F} + \epsilon)$, for each direction ℓ and smallness parameter $\epsilon \ll 1$, and applying either of the minmod $\phi_\ell = \max[0, \; \min(1, \; \theta_\ell)]$, van Leer $\phi_\ell = (|\theta_\ell| + \theta_\ell)/(1 + |\theta_\ell|)$, or superbee $\phi_\ell = \max[\min(1, \; 2\theta_\ell), \; \min(2, \; \theta_\ell)]$ limiters, to derive the final expression for the zone-centered limited gradient components $(\partial_\ell\mathbf{F})_z^L = \phi_\ell\partial_\ell^D\mathbf{F}$.

An alternative, though somewhat more restrictive and costly, method that we have developed for applying unstructured grid limiters on gradient functions is based on modifying the magnitude of the average gradient with some function of the maximum ($\partial_{\max} \equiv \max[|\partial_i^U|, \; |\partial_i^D|, \; |\partial_i^A|]$) and minimum ($\partial_{\min} \equiv \min[|\partial_i^U|, \; |\partial_i^D|, \; |\partial_i^A|]$) of the three sub-zonal gradient magnitudes. For example,

$$(\partial_i\mathbf{F})_z^L = \alpha \; h \, (\beta\partial_{\max}, \; (1 - \beta)\partial_{\min}) \frac{\partial_i^A\mathbf{F}}{|\partial_i^A\mathbf{F}| + \epsilon} \; , \tag{27}$$

where β is a steepness parameter bounded by $0 \leq \beta \leq 1$, $h(...)$ is any function of the arguments, and α is a co-efficient to enforce monotonicity in the extrapolated field $\mathbf{F}_f^*$. In particular, we set $\alpha = \min(1, \; \max(0, \; \min(\alpha_1, \; \alpha_2)))$, where

$$\alpha_1 = \begin{cases} \frac{\max(0, \; \mathbf{F}_{z,n} - \mathbf{F}_z)}{\mathbf{F}_f - \mathbf{F}_z} & \text{if} \quad \mathbf{F}_f = \mathbf{F}_z + (\partial_i \mathbf{F})_z^L (r_f^i - r_z^i)/\alpha > \max(\mathbf{F}_z, \mathbf{F}_{z,n}) \\ 1 & \text{otherwise} \end{cases} \; , \quad (28)$$

and

$$\alpha_2 = \begin{cases} \frac{\min(0, \; \mathbf{F}_{z,n} - \mathbf{F}_z)}{\mathbf{F}_f - \mathbf{F}_z} & \text{if} \quad \mathbf{F}_f < \min(\mathbf{F}_z, \mathbf{F}_{z,n}) \\ 1 & \text{otherwise} \end{cases} \; , \quad (29)$$

where $\mathbf{F}_{z,n}$ refers to the field value in the neighbor zone center. The min/max operations in (28) and (29) are performed over each of the faces in the donor cell, and α is chosen as the smallest value needed for strict monotonicity across all cell faces.

3.1.2. Artificial Viscosity

We have implemented five different artificial viscosity options for shock capturing. All of these constructs have a common inertia multiplier defined for relativistic MHD as

$$I = D + E + W(P + ||Q|| + 2P_B) \; . \quad (30)$$

The inertia is also normalized by a factor I_F that scales out the local 3-geometry in curvilinear coordinates, and introduces a relativistic boost factor to an arbitrary power that is useful for effectively transforming the length scale between proper and boosted frames, and providing a flexible scaling with boost. The normalized inertia multiplier is thus defined as

$$I_N = \frac{I}{I_F} = (D + E + W(P + ||Q|| + 2P_B)) \frac{1}{\sqrt{\gamma}} \left(\frac{\sqrt{-g}}{W} \right)^n \; , \quad (31)$$

where γ is the 3-metric determinant, and n is an arbitrarily specifiable constant.

The simplest artificial viscosity we consider is the scalar form based on the work of von Neumann & Richtmyer (1950):

$$Q_j^i = \begin{cases} I_N \; \Delta l \; \partial_k V^k \; (k_q \; \Delta l \; \partial_k V^k - k_l \; C_s)\delta_j^i & \text{if} \quad \partial_i V^i < 0 \\ 0 & \text{otherwise} \end{cases} \; , \quad (32)$$

where Δl is the minimum covariant zone length, C_s is the local sound speed, and k_q and k_l are constant coefficients multiplying the quadratic and linear contributions, respectively. This scalar viscosity remains one of the most popular representations due to its simplicity and robustness; however, it is also the most diffusive of the methods we have implemented since it indescriminantly filters out transverse, longitudinal, and sheared isotropically averaged compressive flows.

A second option for viscosity is similar to (32) but is designed for anisotropic shock capturing along the principal grid axes similar to what is achieved in directionally split, fully structured mesh approaches:

$$Q_j^i = \frac{I_N \; \Delta l}{2}(k_q \; \Delta l \; \partial_i V^i - k_l \; C_s) \; \text{diag}\left[\partial_x V^x - |\partial_x V^x|, \; \partial_y V^y - |\partial_y V^y|, \; \partial_z V^z - |\partial_z V^z|\right] \; , \quad (33)$$

where diag[...] refers to a list of the main diagonal elements of a tensor. This is generally less diffusive than the isotropic scalar viscosity option since it is automatically disengaged along any grid direction that is not undergoing compression.

Another option is based on the scalar viscosity developed by White (1973), but extended here for relativistic problems. Defining the quantity

$$\widetilde{Q} = \Delta l \ |\partial_i V^i|^{1/2} \ |g^{ij} \partial_i P \ \partial_j(I_N^{-1})|^{1/4} \ , \tag{34}$$

this viscosity can be written as

$$Q_j^i = I_N \ \widetilde{Q} \ (k_q \ \widetilde{Q} + k_l \ C_s)\delta_j^i \tag{35}$$

when both conditions, $g^{ij}\partial_i P \ \partial_j(I_N^{-1}) < 0$ and $\partial_i V^i < 0$, are met. The advantage of (35) is that both pressure and velocity gradients are incorporated into its definition, which is a better indication of the presence of shocks than the velocity gradient by itself. It can therefore be more effective at suppressing artificial heating in regions undergoing adiabatic compression.

The final two options we consider are genuine tensor viscosities. The first of these is similar to Tscharnuter & Winkler (1979), but does not include the full covariant gradient treatment. However, since the velocity gradients are computed in the conformal frame and the proper volume is accounted for in the inertia normalization, the version we have implemented

$$Q_j^i = I_N \ \Delta l \ (k_q \ \Delta l \ \partial_i V^i - k_l \ C_s) \ \mathrm{Sym} \left(\partial_j V^i - \frac{\partial_i V^i}{3}\delta_j^i \right) \ , \tag{36}$$

where $\mathrm{Sym}(...)$ denotes a symmetry operation, is a reasonable simplification. This traceless tensor viscosity generally outperforms scalar viscosities in preserving geometric symmetries (e.g., sphericity), and suppressing viscous heating in homologous spherical contraction.

The last option we consider is potentially the least diffusive, but also the most unstable or unpredictable method due to the matrix inversion operations needed to align the viscosity calculation to the natural principal axes of the shock frame. The shock orientation and velocity differences are determined by the eigenvectors $R_k^i(S)$ and eigenvalues $\lambda^i(S)$ of the symmetrized strain rate tensor $S_j^i = \mathrm{Sym}(\partial_j V^i - \partial_i V^i \ \delta_j^i/3)$. In this procedure the artificial viscosity is written as

$$Q_j^i = R_k^i(S) \ \widehat{Q}_l^k \ R_j^l(S)^T \ , \tag{37}$$

where $R_j^l(S)^T$ is the transpose of $R_k^i(S)$, $\widehat{Q}_l^k$ is the usual von Neumann-Richtmyer viscosity in the shock aligned frame where the viscosity tensor has only diagonal elements

$$\widehat{Q}_i^i = I_N \ \widehat{\Delta l}^i \ \lambda^i(S) \ \left(k_q \ \widehat{\Delta l}^i \ \lambda^i(S) - k_l \ C_s\right) \ . \tag{38}$$

The shock-aligned length scales $\widehat{\Delta l}$ are computed in a similar fashion, also accounting for local proper frame metric distortions, $M_{ij} = g_{ij}\Delta x^i \Delta x^j$ (assuming no index summation here). Representing the eigenvalues and eigenvectors of the matrix M_{ij} as $\lambda^i(M)$ and $R_{ij}(M)$, we define the shock-aligned length scales as the diagonal elements of the transformed length scale tensor $\widehat{\Delta l}^i = \mathrm{diag}[\widehat{\Delta l}_{ij}]$, where

$$\widehat{\Delta l}_{ij} = R_{ia}(S)^T \ R_{ab}(M) \ \sqrt{\lambda^{bc}(M)} \ R_{cd}(M)^T \ R_{dj}(S) \ , \tag{39}$$

and $\lambda^{bc}(M)$ is the diagonal tensor of eigenvalues $\lambda^i(M)$. This expression effectively transforms the principal length scales $\lambda^i(M)$ to the grid axes, then to the principal frame of the strain rate tensor.

Because the basic strain rate tensor (and especially velocity divergence) does not always distinguish between discontinuous shocks and smooth compressive flows, it is sometimes necessary to be more selective about where artificial viscosity is applied. As an option we can modify the strain rate tensor as

$$\partial_i V^j \Rightarrow \partial_i V^j - k_L \ \partial_i^L V^j \ , \tag{40}$$

where k_L is a constant less than unity (typically 0.5), and ∂_i^L is a limited gradient. This effectively reduces the viscosity levels over smooth flows where the limiter has no affect, while keeping it strongly active over shocks where the limited gradient vanishes. In this case we use a hard limiter and set $\partial_i^L V^j = 0$ if any of the velocity or velocity gradient components have opposite signs across any of the nearest neighbor zones. If both the velocity and its gradient are monotonic in the local neighbor patch, we set $\partial_i^L V^j = \partial_i V^j$.

3.2. NOCD Method

We take a slightly different and significantly simpler approach in this paper to solving the fully conservative system of equations described in §2.2 than the Riemann-free method we implemented in *Cosmos* (Anninos & Fragile 2003). This approach, developed by Kurganov & Tadmor (2000), is also part of the NOCD family of solutions, but we find it to be generally less diffusive and less sensitive to Courant restrictions.

The curvature sources in equations (15) and (16) are updated using second order finite volume discretization, and a first order in time Euler advance method. The divergence terms in (15), (16) and (21) are updated in time from u^n to u^{n+1} using a general Nth order method consisting of a sequence of first order Euler steps (Shu & Osher 1988). Writing the time update in terms of forward Euler templates, high order time solutions can be expressed as

$$
\begin{aligned}
u^{(1)} &= u^n + \Delta t^n S(u^n) \ , \\
u^{(m+1)} &= \eta_m u^n + (1 - \eta_m)(u^{(m)} + \Delta t^n \ S(u^{(m)})) \ , \\
u^{n+1} &= u^k \ ,
\end{aligned}
\tag{41}
$$

for ordered sequences $m = 1, \ 2, \ ..., \ k - 1$ up to k steps, an arbitrary source term $S(u)$, and constant parameters

$$
\eta = \begin{cases} (1/2, \ -) \ , & \text{2nd order} \\ (3/4, \ 1/3) \ , & \text{3rd order} \end{cases} \ .
\tag{42}
$$

At first order, η_m is not used since that reduces to a simple, single-step forward Euler solver. The time update is thus conveniently solved as a sequence of first order Euler cycles, and is easily extended to higher order using these simple prescriptions.

In semi-discrete form, the single-step solution to a general nonlinear convection equation for a general field ω, representing the energy (15), momentum (16), or induction (21) equations, is written in finite volume form as

$$
\partial_t \omega = -\partial_i F^i(\omega) = \frac{1}{V_z} \sum_f^{\text{faces}} \left[\frac{1}{2} \left(F_f^i(\omega_f^-) + F_f^i(\omega_f^+) \right) (A_i)_f - \frac{a_f}{2} \left(\omega_f^- - \omega_f^+ \right) ||A_f|| \right] \ ,
\tag{43}
$$

where F^i are the numerical fluxes, $a_f = \max(a_f^+, \ a_f^-)$ is the maximum local propagation speed, and $\omega_f^\pm = \omega_\pm + (\partial_i \omega)_\pm^L \ (r_f^i - r_\pm^i)$ are the limited gradient projections of the cell-centered field $\omega_\pm$ to the cell faces. The subscripts $\pm$ refer to either the donor cell center $(-)$ or the opposite zone $(+)$ across face f, and the superscripts $\pm$ refer to the face centered projections of the field originating from the corresponding zone. In this approach, the transport terms are grouped together with the other fluxes, and the discrete solution (43) is applied to all divergence source terms (transport included) simultaneously.

3.3. Extended AV Method

The basic internal energy formulation with artificial viscosity can be expanded easily to include an additional equation for the conserved energy in the form (15). The general idea in this dual energy approach is to extract the thermal component from the total energy, and depending on the accuracy of the result, use it to over-write the solution computed directly from the internal energy evolution equation. However, care must be used when extracting the internal energy, since it is often the case that adiabats in total energy conserving methods can be grossly miscalculated.

In this scheme, the total energy is used as an option to compute the four-momentum normalization at various stages of the solve sequence, as well as the inertia for the artificial viscosity when certain conditions are met. Defining $\mathcal{E}_D$ as the non-thermal or "dynamical" component of the conservative energy,

$$\mathcal{E}_D = \frac{DW}{\sqrt{-g}} + \frac{2P_B W^2}{\sqrt{-g}} + \sqrt{-g}\left(g^{00}P_B - \frac{B^0 B^0}{4\pi}\right) ,\tag{44}$$

we write

$$\widetilde{E} = \frac{(\mathcal{E} - \mathcal{E}_D)\sqrt{-g}\,W}{\Gamma W^2 + (\Gamma - 1)g^{00}(\sqrt{-g})^2} ,\tag{45}$$

for the internal energy extracted from the conserved energy field, and

$$\begin{aligned} I &= W(\rho h + 2P_B) = D + E + W(P + \|Q\| + 2P_B) \\ &= \frac{\sqrt{-g}}{W}\left(\mathcal{E} - \sqrt{-g}g^{00}(P + P_B) + \frac{1}{4\pi}\sqrt{-g}B^0 B^0\right) \end{aligned}\tag{46}$$

for the inertia and momentum normalization.

Also, an additional term is added to the total energy evolution equation that accounts for collisional dissipation heating arising from the artificial viscosity. The conservative energy equation that we solve takes the general form

$$\partial_t \mathcal{E} + \partial_i\left(\mathcal{E}V^i\right) + \partial_i\left(F^i\right) = \Sigma^0 ,\tag{47}$$

where the flux F^i is now defined as

$$F^i = \sqrt{-g}\left((g^{0j} - g^{00}V^j)\left((P + P_B)\delta_j^i + Q_j^i\right) - \frac{1}{4\pi}(B^i B^0 - B^0 B^0 V^i)\right) .\tag{48}$$

Although we use essentially the same equation for energy (apart from Q_j^i) as the NOCD method described in the previous section, we solve it using a different, more conventional operator split approach. Here we solve sequentially for curvature effects ($\partial_t \mathcal{E} = \Sigma^0$), followed by the transport source ($\partial_t \mathcal{E} + \partial_i(\mathcal{E}V^i) = 0$) which is updated synchronously with the momentum, internal energy, and magnetic induction advection, then finally we apply second order finite volume discretization to evaluate the remaining flux divergence term ($\partial_t \mathcal{E} + \partial_i F^i = 0$).

The final step in this extended scheme is to determine whether the total energy solution is known well enough to extract accurately the internal energy. We use for a measure of accuracy, the minimal difference ratio

$$\left(\frac{\delta\mathcal{E}}{\mathcal{E}}\right)_{\min} \equiv \frac{\min[E\,h(\Gamma),\ \max(\rho\epsilon_{\text{floor}}W h(\Gamma),\ \widetilde{E}\,h(\Gamma))]_N}{\max(\mathcal{E})_N} ,\tag{49}$$

where

$$h(\Gamma) = \frac{\Gamma W^2 + (\Gamma - 1)g^{00}(\sqrt{-g})^2}{\sqrt{-g}\,W} ,\tag{50}$$

$\rho\epsilon_{\mathrm{floor}}$ is the minimum allowable energy density threshold, and the subscript N refers to extending local minimum and maximum calculations to include all neighbor zones, adding an extra measure of safety. A common problem with total energy schemes in general is that numerical truncation errors can accumulate to the point that the sum of different physical contributions often exceeds the total energy ($\mathcal{E}_D > \mathcal{E}$), especially in kinematic or magnetic field dominated flows, and in the vicinity of strong shocks. This problem is avoided by forcing a minimum threshold on either E or $\widetilde{E}$ to guarantee positivity, and by preserving the solution from the internal energy equation whenever $\mathcal{E}_D \geq \mathcal{E}$, or $(\delta\mathcal{E}/\mathcal{E})_{\min} \leq \delta_c$, where δ_c is a user defined parameter large enough to prevent numerical noise from corrupting the solution. The internal energy is otherwise set to $E = \max(\epsilon_{\mathrm{floor}}W, \widetilde{E})$ when $(\delta\mathcal{E}/\mathcal{E})_{\min} > \delta_c$ and the extracted thermal component can be trusted.

4. Code Tests

4.1. Hydrodynamics

4.1.1. Shock Tube

We begin testing with one of the standard problems in fluid dynamics, the shock tube, in which two different fluid states are initially separated by a membrane. At $t = 0$ the membrane is removed and the fluid evolves in such a way that five distinct regions appear in the flow: an undisturbed region at each end, separated by a rarefaction wave, a contact discontinuity, and a shock wave. Although this problem only checks the hydrodynamic elements of the code, as it assumes a flat background metric and ignores magnetic fields (magnetosonic shocks will be considered in §4.2), it is still useful for evaluating the shock-capturing properties of the different methods. We consider the high boost ($W = 3.59$, $\Gamma = 5/3$) case from Anninos & Fragile (2003). The initial state is specified as $\rho_L = 1$, $P_L = 10^3$, $V_L = 0$ to the left of the membrane and $\rho_R = 1$, $P_R = 10^{-2}$, $V_R = 0$ to the right. The membrane is located at $x = 0.5$ on a grid of unit length. The results presented here are run using the scalar artificial viscosity with a quadratic viscosity coefficient $k_q = 2.0$, linear viscosity coefficient $k_l = 0.3$, Courant factor $k_{cfl} = 0.3$, viscosity multipier $k_{\dot{W}} = 0$, and are carried out on fixed, uniform grids of differing resolutions in order to establish the convergence of each method. Figures 1, 2, and 3 show spatial profiles of the results at time $t = 0.36$ on a grid of 800 zones using the AV, eAV, and NOCD methods, respectively. Table 1 summarizes the errors in the primitive variables ρ, P, and V for four different grid resolutions (400, 800, 1600, and 3200 zones) and the three different CFD methods (AV, eAV, and NOCD) using the L-1 norm (i.e., $\|E(a)\|_1 = \sum_{i,j,k} \Delta x_i \Delta y_j \Delta z_k |a_{i,j,k}^n - A_{i,j,k}^n|$, where $a_{i,j,k}^n$ and $A_{i,j,k}^n$ are the numerical and exact solutions, respectively, and for one-dimensional problems the orthogonal grid spacings are set to unity). All three methods converge at approximately first order as expected for this class of problem, and the errors are consistent with those reported for our previous code (Anninos & Fragile 2003).

4.1.2. Shock Collision

A second test presented here is the wall shock problem involving the shock heating of cold fluid hitting a wall at the left boundary ($x = 0$) of a unit grid domain. The initial data are set up to be uniform across the grid with adiabatic index $\Gamma = 4/3$, pre-shocked density $\rho_1 = 1$, pre-shocked pressure $P_1 = (\Gamma - 1) \times 10^{-8}$, and velocity $V_1 = -v_{init}$. When the fluid hits the wall a shock forms and travels to the right, separating the
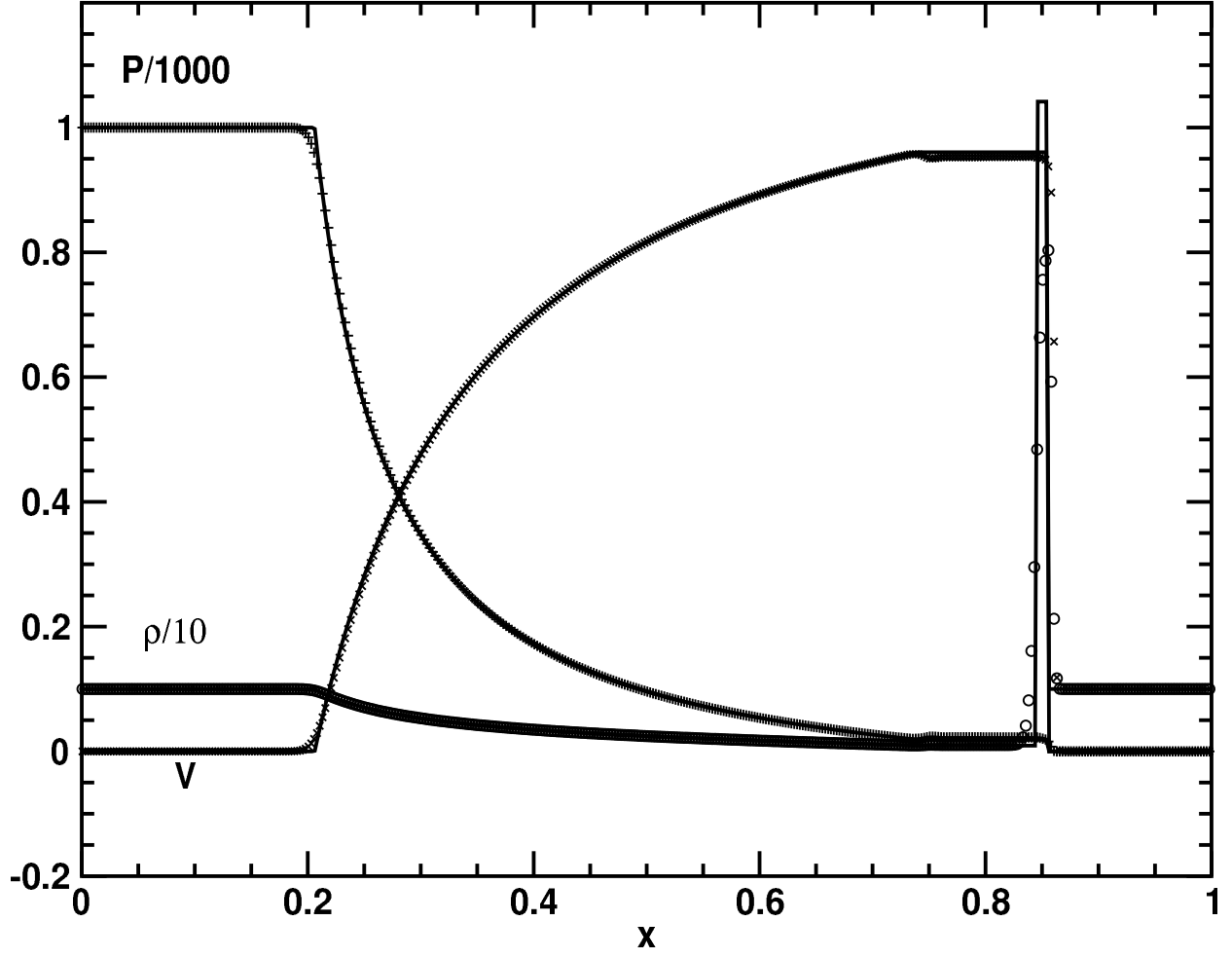
Fig. 1.— Results at time $t = 0.36$ for the shock tube test using artificial viscosity (AV) and 800 zones. The data points in this plot have been sampled to reduce overcrowding. Only 400 points are shown. The solid line shows the analytic solution.

initial pre-shocked conditions from the post-shocked state $(\rho_2,\ P_2,\ V_2)$ with solution in the wall frame

$$V_S = \frac{\rho_1 W_1 V_1}{\rho_2 - \rho_1 W_1}, \tag{51}$$

$$P_2 = \rho_2(\Gamma - 1)(W_1 - 1), \tag{52}$$

$$\rho_2 = \rho_1 \left[\frac{\Gamma + 1}{\Gamma - 1} + \frac{\Gamma}{\Gamma - 1}(W_1 - 1) \right], \tag{53}$$

where V_S is the velocity of the shock front, and the pre-shocked energy and post-shocked velocity are both assumed negligible $(\epsilon_1,\ V_2) \to 0$. All of the results in this section are performed on a 200 zone uniformly-spaced mesh and run to a final time of $t = 2.0$. For the AV and eAV methods, we use the scalar viscosity with $k_q = 2.0$ and $k_l = 0.7$. The Courant factor is set to $k_{cfl} = 0.3$ for all methods.

Figure 4 plots the mean-relative errors in density, which are generally greater than errors in either the pressure or velocity, as a function of boost factor. Although we are not able to extend the AV method
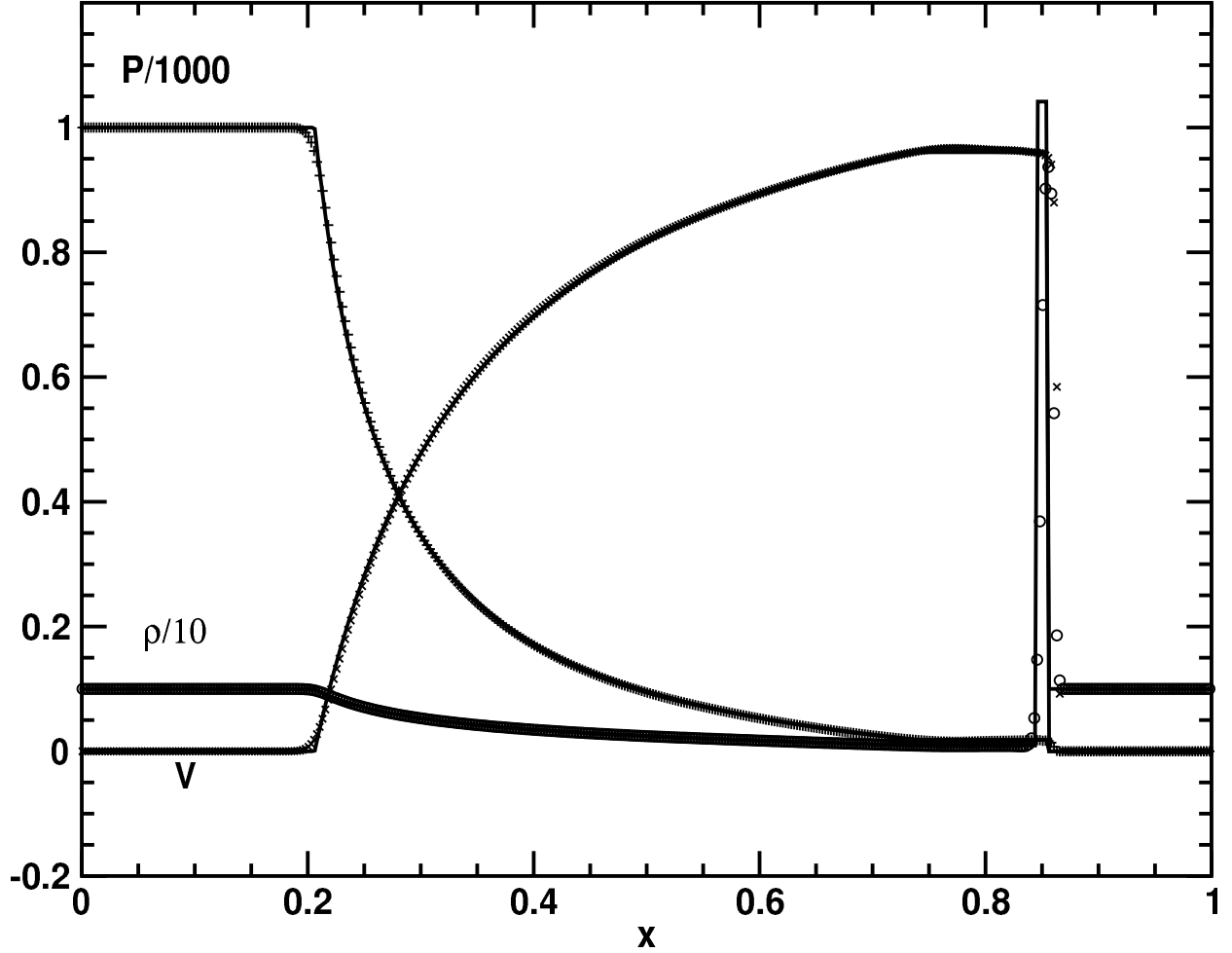
Fig. 2.— As Figure 1 but with the extended viscosity (eAV) scheme.

reliably (which we define by a 10% mean error threshold and increased sensitivity to viscosity parameters) beyond $v_{init} \sim 0.95$, the eAV and NOCD methods are substantially more robust. As shown in Figure 5, both methods can be run up to arbitrarily high boost factors ($v_{init} > 0.99999$) with mean relative errors typically remaining below 2% with no significant increasing trend. As noted previously (Anninos & Fragile 2003), the errors for the AV method can be improved significantly by either lowering the Courant factor or increasing the viscosity coefficients. However, the sensitive dependence on these parameters detracts considerably from the attractiveness of this method for this class of problem. The errors for the eAV method can also be improved by adjusting the viscosity coefficients, although we find that it performs well even with the "standard" values used here.

4.1.3. Boosted Shock Collision

An elaboration of the wall shock problem from the previous section is the collision of two boosted fluids. The fluids flow toward each other and collide, each shocking against the other and forming a contact
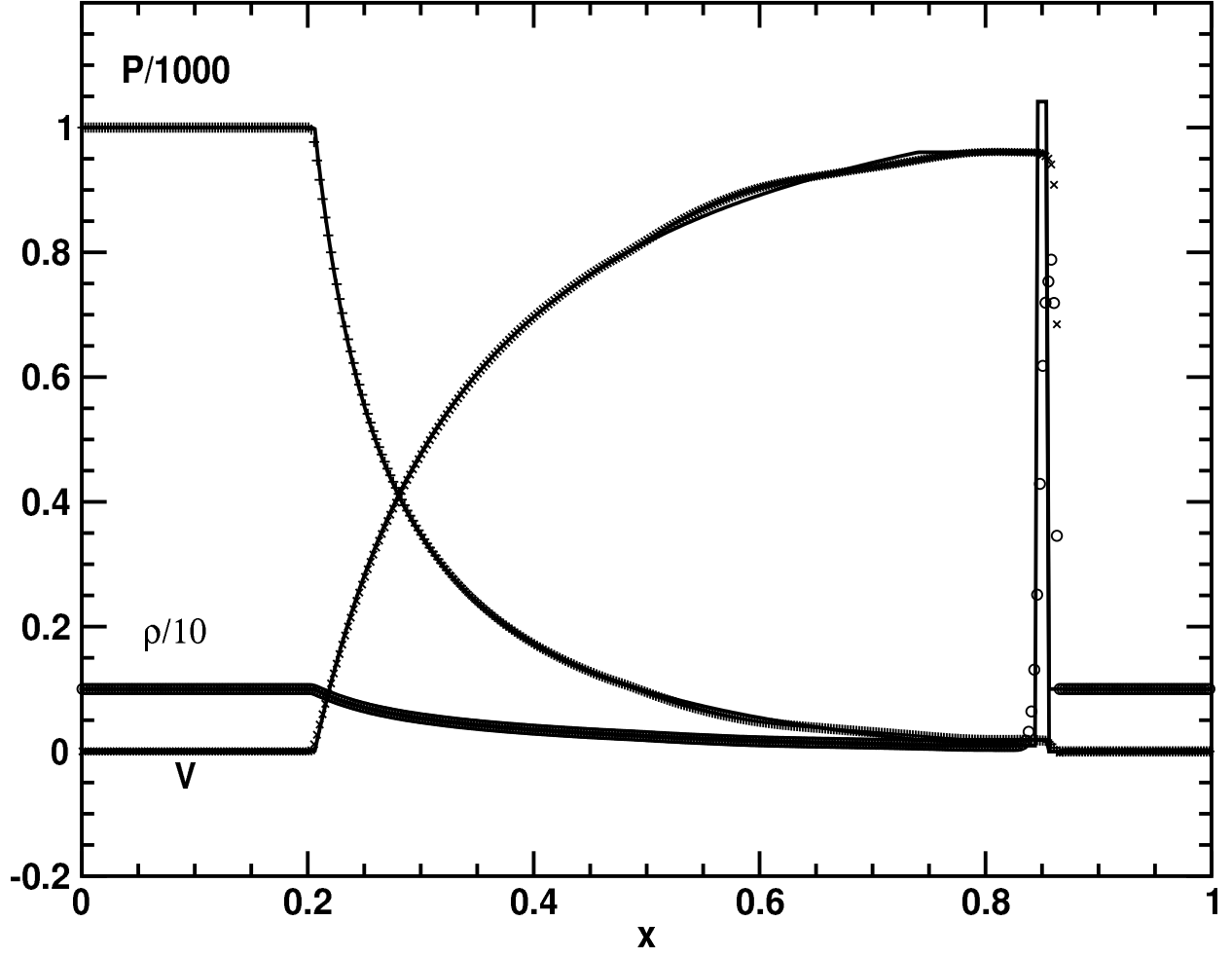
Fig. 3.— As Figure 1 but with the non-oscillatory central difference (NOCD) scheme.

discontinuity. In the center-of-momentum frame, in which the contact discontinuity between the fluids is stationary, this system is equivalent to a pair of opposing wall shocks, each impinging on the other. However, by boosting this system's center-of-momentum frame with respect to the grid frame, one devises a very rigorous test of the Lorentz invariance of the code under nonsymmetric conditions, with multiple jump discontinuities and highly relativistic shock velocities.

In the center-of-momentum (primed) frame, a fluid with initial state $(\rho_1,\ P_1,\ V_1' > 0)$ flows from the left boundary while a fluid of state $(\rho_4,\ P_4,\ V_4' < 0)$ flows from the right; we assume each fluid is cold: $P_1 = P_4 = 0$. Upon collision, fluid 1 is shocked into a state $(\rho_2,\ P_2,\ V_2')$ while fluid 4 is shocked into state $(\rho_3,\ P_3,\ V_3')$, where the fluids are numbered sequentially from left to right. In this frame, each shocked fluid comes to rest; $V_2' = V_3' = 0$. This implies force equilibrium between these fluids; $P_2 = P_3$. Using equations (52) and (53), pressure balance gives

$$\rho_1(\Gamma W_1' + 1)(W_1' - 1) = \rho_4(\Gamma W_4' + 1)(W_4' - 1) \ . \tag{54}$$

The proper densities of the shocked fuids (from eqn. 53) are

$$\rho_2 \;=\; \rho_1 \frac{\Gamma W_1' + 1}{\Gamma - 1} \tag{55}$$

$$\rho_3 \;=\; \rho_4 \frac{\Gamma W_4' + 1}{\Gamma - 1} \;, \tag{56}$$

and the specific energies are (e.g. Hawley et al. 1984)

$$\epsilon_2 \;=\; W_1' - 1 \tag{57}$$

$$\epsilon_3 \;=\; W_4' - 1 \;. \tag{58}$$

Pressure balance again implies $\rho_2 \epsilon_2 = \rho_3 \epsilon_3$. Also, from equation (51) the reverse shock velocity, V_r', between materials 1 and 2, and the forward shock velocity, V_f', between fluids 3 and 4 are expressed as

$$V_r' \;=\; -\frac{(W_1' - 1)(\Gamma - 1)}{W_1' V_1'} \tag{59}$$

$$V_f' \;=\; -\frac{(W_4' - 1)(\Gamma - 1)}{W_4' V_4'} \;. \tag{60}$$

Typically the grid (lab frame) velocities V_1 and V_4 are known and the velocity of the center-of-momentum frame and contact discontinuity, V_d, must be solved for numerically by substituting the boost transformations

$$W_1' = W_d W_1 (1 - V_1 V_d) \;, \quad W_4' = W_d W_4 (1 + V_4 V_d) \tag{61}$$

into equation (54), where $W_i = (1 - V_i^2)^{-1/2}$. The system can also be boosted into a desired frame by standard velocity addition.

Figures 6, 7 & 8 compare the analytic and numerical solutions, using the eAV method, for three examples of boosted collisions. We find very good agreement to the solutions (Table 2) when the opposing primed-frame momenta of each fluid is symmetric (Figure 6), asymmetric (Figure 7) and for a more extreme relativistic case with Lorentz factors of about 100 (Figure 8). Fractional errors for density in the shocked region are typically $\Delta \rho / \rho \sim 10^{-4}$ while both proper energy and boost factor fractional errors are of order 10^{-5}. The tail in mass density on the downwind (right hand) side of the shocked region is a small proportion (3% for Figures 6 & 7 and 1% for Figure 8) of the total shocked mass and converges to zero with increased zoning. The NOCD method also gives good agreement, but tends to be slightly more diffusive, with a larger mass tail on the trailing shock. In the most extreme relativistic case, shown in Figure 8, the numerical results are slightly behind (to the right of) the analytical solution, corresponding to temporal delay in the onset of the numerical shock of $\Delta t \approx 10^{-4}$. These highly relativistic shocks require very fine zoning and thus AMR is extensively used in order that these runs be computationally feasible. Up to 12 levels of refinement are used in the highest boost test. In these examples a simple density threshold is used, above which refinement is triggered; however, more complex (and efficient) triggering methods such as discussed in the next section have also been successfully employed.

4.1.4. Blast Waves

A further application of the ultra-relativistic capabilities of the eAV and NOCD methods demonstrated in the previous section and one that is of particular astrophysical significance is the relativistic blastwave.

Much like its Newtonian counterpart, the Sedov-Taylor blastwave (e.g. Landau & Lifshitz 1959), there is a self-similar analytical solution for the ultra-relativistic blastwave, first described by Blandford & McKee (1976).

The analytical solution of Blandford & McKee (1976) depends on the initial total energy in the blastwave, E_{BM}, the Lorentz factor with which its shock front initially expands, γ_{BM}, and the ambient density, ρ_{BM}, into which it expands. From these one can define an initial radius of the blastwave

$$r_{\mathrm{BM}} \equiv \left(\frac{17 E_{\mathrm{BM}}}{8 \pi \gamma_{\mathrm{BM}}^2 \rho_{\mathrm{BM}}} \right)^{1/3} . \tag{62}$$

The solution for radii, $0 < r < r_{\mathrm{BM}}$, is based on the similarity variable

$$\chi(r) \equiv 1 + 8 \gamma_{\mathrm{BM}}^2 (1 - r/r_{\mathrm{BM}}) . \tag{63}$$

The coordinate density and energy, as used by *Cosmos++* , and the Lorentz factor are

$$D(r) = 2\sqrt{-g}\rho_{\mathrm{BM}}\gamma_{\mathrm{BM}}^2 \chi(r)^{-7/4} \tag{64}$$

$$E(r) = \sqrt{-g}\rho_{\mathrm{BM}}\gamma_{\mathrm{BM}}^2 (\sqrt{2}\gamma_{\mathrm{BM}}\chi(r)^{-23/12} - 2\chi(r)^{-7/4}) \tag{65}$$

$$\gamma(r) = \sqrt{1 + \frac{\gamma_{\mathrm{BM}}^2}{2\chi(r)}} \tag{66}$$

where we have interpreted equation (29) of Blandford & McKee (1976) as the radial component of the 4-velocity in order that $\gamma \geq 1$. For all $r > r_{\mathrm{BM}}$, $D(r) = \sqrt{-g}\rho_{\mathrm{BM}}$, $\gamma(r) = 1$ and the energy is set to a numerically insignificant value, typically $E(r) = 10^{-4}D(r)$.

The relativistic blastwave is characterized by a very thin, $\Delta r \propto r_{\mathrm{BM}}/(8\gamma_{\mathrm{BM}}^2)$ [eqn. 63], shell of matter and energy rapidly expanding into an external medium. Very fine zoning is required to resolve the shell, while relatively few zones are necessary in the vacuous bubble enclosed by the shell or the external medium. Thus this problem is ideally suited for adaptive mesh refinement. For example, a blastwave with an initial Lorentz factor of $\gamma_{\mathrm{BM}} = 10$ would require 800 zones across its radius just to ensure that the shell is represented by a single zone. Because of the steep gradients behind the shock, to *resolve* the shell requires $f_{\mathrm{res}} \sim 100$ times as many zones, which becomes a large computational problem. This is compounded by the fact that typical simulations evolve the blastwave over distances $\propto r_{\mathrm{BM}}$, thus requiring about $r_{\mathrm{BM}}/\Delta r \sim r_{\mathrm{BM}} f_{\mathrm{res}}/(k_{cfl}\Delta t) \sim 800 f_{\mathrm{res}}/k_{cfl} \sim 10^6$ time steps, where k_{cfl} is the Courant factor. For $\gamma_{\mathrm{BM}} > 10$, stability typically requires $k_{cfl} \sim 0.1$. Therefore adaptive mesh refinement, with zones concentrated into the shell, is a practical necessity for relativistic blastwaves.

The relativistic blastwave, with its thin shell, steep gradients, and sharp cusp at the shock front, is challenging to simulate. The method developed for these problems is to refine a zone if any of three criteria are met: First, all zones for which the density $\rho > f_{\mathrm{thresh}}\rho_{\mathrm{max}}$ are refined to the fullest allowable extent, where typically $f_{\mathrm{thresh}} = 0.9$. This condition is required to keep the cusp at the shock front as resolved as possible. Second, the normalized derivative of the proper density field, $(\Delta x/\overline{\rho})\nabla\rho$, must remain below a threshold, where Δx is the zone size and $\overline{\rho}$ is the average value. This is effective at maintaining the steep gradient behind the shock. Finally, the normalized curvature of this field, $\Delta x|\nabla^2\rho|/|\overline{\nabla\rho}|$, must remain below a maximum threshold. This condition puts zones ahead of the advancing shock due to the high curvature at the shock discontinuity, and also smooths the regions tagged by slope. If $\rho < f_{\mathrm{thresh}}\rho_{\mathrm{max}}$ and both normalized slope and curvature of a zone fall below their respective thresholds, then that zone is tagged for derefinement.

As shown in Figure 9, *Cosmos++* is able to evolve a blastwave with $E_{\mathrm{BM}} = 10^{51}$ ergs from an initial Lorentz factor of $\gamma_{\mathrm{BM}} = 30$ to a non-relativistic blastwave. Such a simulation is demanding, requiring $\sim 10^6$ cycles to evolve the relativistic phase. This simulation is evolved on a base mesh of 100 zones with initially 17 levels of allowed refinement. The number of allowed refinement levels is periodically decremented nine times as the blastwave decelerates and broadens. Thus only eight levels of refinement are employed during the non-relativistic phase. As a result, the time step during the final non-relativistic phase is $2^{10} \approx 1000$ times larger than the initial timestep.

Figure 10 shows the self-similarity of the relativistic and non-relativistic phases of the blastwave evolution by scaling and super-imposing several density profiles for each phase. One can see excellent agreement with the analytical solution in both cases. For the relativistic phase, the eAV method (shown in the left plot) tends to more robustly evolve the analytical solution, with less sensitivity to time step or AMR refinement prescriptions. However, the NOCD method (shown in the right plot) more reliably transitions to the non-relativistic limit; for instance capturing the shock discontinuity in density with $\sim 1\,\%$ accuracy as opposed to $\sim 10\,\%$ accuracy for the eAV method. This might be due to the enforced energy conservation of the NOCD method. The eAV method typically only loses $1 - 2\%$ of the total energy over the course of the evolution, but this may occur primarily in the shocked shell, thus causing a slight drift in the solution.

4.2. Magnetohydrodynamics

4.2.1. Alfvén Wave Propagation

The class of linear Alfvén waves described by De Villiers & Hawley (2003a) provide an excellent test of the method of characteristics for magnetic fields subject to transverse or shearing mode perturbations. Considering a general wave function $f(x - v_A^{\pm} t)$, solutions to the linear perturbation equation with a fixed background field $\mathcal{B}^x$ and constant velocity V^x in Minkowski spacetime yields for the transverse components

$$V^y(x,t) = \left(\frac{1 - \zeta\chi}{2}\right) f(x - v_A^- t) + \left(\frac{1 + \zeta\chi}{2}\right) f(x - v_A^+ t) , \tag{67}$$

$$\mathcal{B}^y(x,t) = \frac{\zeta}{2} \left[f(x - v_A^- t) - f(x - v_A^+ t) \right] , \tag{68}$$

with parameters

$$\zeta = \frac{\mathcal{B}^x (1 + \eta^2)}{\eta \sqrt{\eta^2 + W^{-2}}} , \quad \eta^2 = \frac{||B||^2}{4\pi\rho h W^2} , \quad \chi = -\frac{\eta^2 V^x}{\mathcal{B}^x(1 + \eta^2)} , \quad \beta = \frac{8\pi P}{||B||^2} , \tag{69}$$

and Alfvén speed

$$v_A^{\pm} = \frac{V^x \pm \eta\sqrt{\eta^2 + W^{-2}}}{1 + \eta^2} \xrightarrow[V^x = 0]{} \sqrt{\frac{||B||^2}{4\pi\rho h + ||B||^2}} = \sqrt{\frac{2(\Gamma - 1)\epsilon}{\beta(1 + \Gamma\epsilon) + 2(\Gamma - 1)\epsilon}} . \tag{70}$$

We consider two cases of linear Alfvén waves: a stationary background ($V^x = 0$, case A) in which the pulses travel in opposite directions with equal amplitudes, and a moving background ($V^x = 0.1c$, case B) where the pulses split into asymmetrical waves. These two cases correspond to Models ALF1 and ALF3 of De Villiers & Hawley (2003a). In both cases, the fluid is initialized with a uniform density $\rho = 1$, specific energy $\epsilon = 10^{-2}$, and adiabatic index $\Gamma = 5/3$. The transverse magnetic field components ($\mathcal{B}^y = \mathcal{B}^z$) are initially zero. The longitudinal magnetic field component ($\mathcal{B}^x$) is set by our choice of β ($\beta = 0.001$ for case A and

0.01 for case B). The transverse velocity is initialized with a square pulse: $V^y = 10^{-3}$ for $1 < x < 1.5$, $V^y = -10^{-3}$ for $1.5 \leq x < 2$, and zero elsewhere. The problem is run on a grid 3 units in length.

For case A, the Alfvén velocities are $|v_A^\pm| = 0.963$ ($W = 3.76$); for case B, $v_A^+ = 0.792$ ($W^+ = 1.64$) and $v_A^- = -0.705$ ($W^- = 1.41$). Figure 11 shows the numerical results for the artificial viscosity (AV) method on a grid with 1024 zones overlaid with the analytic solution. The eAV method gives identical results for this test and is not shown. The errors in the plateaus for the stationary background case (case A) are extremely small ($< 0.005\%$); for the moving background (case B), the errors are somewhat larger, though still quite small ($< 0.1\%$)

4.2.2. Magnetosonic Shock Tube

Next we perform another set of numerical shock tube tests, this time including magnetic fields. Similar to the hydrodynamic shock tube test, these problems combine strong shocks and rarefaction features, thus fully stressing the code in the limit of flat space. We initialize two versions of this test, both from Komissarov (1999). In the first test, the initial state is specified as $\rho_L = 1$, $P_L = 10^3$, $V_L = 0$, $\mathcal{B}_L^x = 1$, $\mathcal{B}_L^y = \mathcal{B}_L^z = 0$ to the left of the membrane and $\rho_R = 0.1$, $P_R = 1$, $V_R = 0$, $\mathcal{B}_R^x = 1$, $\mathcal{B}_R^y = \mathcal{B}_R^z = 0$ to the right. Note that since the magnetic field in this case is parallel to the flow and continuous across the discontinuity, it should not play a dynamical role. In this sense, the problem is really a hydrodynamical shock tube similar to the one considered in §4.1.1. Nevertheless, this test appears frequently in the literature and is worth reproducing here to confirm consistency in the MHD solver. For the second test, the initial state is $\rho_L = 1$, $P_L = 30$, $V_L = 0$, $\mathcal{B}_L^y = 20$, $\mathcal{B}_L^x = \mathcal{B}_L^z = 0$ to the left of the membrane and $\rho_R = 0.1$, $P_R = 1$, $V_R = 0$, $\mathcal{B}_R^x = \mathcal{B}_R^y = \mathcal{B}_R^z = 0$ to the right. Here, the initial discontinuity of the field allows it to play a dynamical role in the rarefaction and contact wave regions. These tests are run using the scalar artificial viscosity with a quadratic viscosity coefficient $k_q = 2.0$, Courant factor $k_{cfl} = 0.3$, and are evolved on fixed, uniform grids. Case 1 uses a linear viscosity coefficient $k_l = 0.3$, whereas case 2 does not use the linear term ($k_l = 0$). We do not calculate the analytic solutions for these tests, although a direct comparison can be made between our Figures 12, 13, and 14, and Figure 6 of Komissarov (1999) since we use the same resolution (400 and 500 zones for shock tubes 1 and 2, respectively) as that work. We point out that our different methodologies all give similar results as the Godunov-type scheme used in Komissarov (1999), showing many of the same pathologies (the small post-shock features in shock tube 1 and the kink at the rarefaction edge in shock tube 2), although our AV and eAV methods appear to do better at capturing the density plateau in the Lorentz-contracted shell of material immediately behind the shock.

4.2.3. Bondi Flow

As a test of hydrodynamic and MHD flows in spacetimes with nontrivial curvature, we first consider radial accretion onto a compact, strongly gravitating object, in this case a Schwarzschild black hole. The analytic solution (Michel 1972) is characterized by a critical point in the flow as

$$(u_c^r)^2 = M/2r_c , \tag{71}$$

$$V_c^2 = (u_c^r)^2/[1 - 3(u_c^r)^2] = \frac{(1+n)T_c}{n[1 + (1+n)T_c]} , \tag{72}$$

where u^r is the radial component of the fluid 4-velocity, V_c is the sound speed at the critical point, M is the mass of the black hole, $n = 1/(\Gamma - 1)$ is the polytropic index, and $T = P/\rho$. The remainder of the flow is

described through the equations

$$T^n u^r r^2 \;=\; C_1 \; , \tag{73}$$

$$[1 + (1+n)T]^2 \left[1 - \frac{2M}{r} + (u^r)^2 \right] \;=\; C_2 \; . \tag{74}$$

Following Hawley et al. (1984), we fix C_1 and C_2 by choosing the critical radius of the solution $r_c = 8GM/c^2$ and fixing $\Gamma = 4/3$. We also fix the density at the critical radius (ρ_c) such that $\dot{M} = 4\pi r_c^2 \rho_c u_c^r = -1$.

The physical domain of our simulation extends from $r = 0.98 r_{BH}$ to $r = 20 GM/c^2$, where $r_{BH} = 2GM/c^2$ is the radius of the black-hole horizon. Here we use Kerr-Schild coordinates, which allow us to place the inner boundary of the computational domain inside the horizon. The radial coordinate is replaced by a logarithmic coordinate $\eta = 1 + \ln(r/r_{BH})$, and the problem is evolved over a time interval $\Delta t = 100 GM/c^3$. We measure the convergence of our solution at four different resolutions (32, 64, 128, and 256 zones) using the one-dimensional L-1 norm of ρ. For 256 zones, the respective errors for the AV, eAV, and NOCD methods are 1.14×10^{-3}, 1.08×10^{-3}, and 4.66×10^{-4}. The convergence rates are between first and second order: 1.3, 1.4, and 1.4 for the AV, eAV, and NOCD methods, respectively. These rates are generally consistent with the convergence reported by De Villiers & Hawley (2003a).

We can extend this test to the GRMHD regime by adding a radial magnetic field. Inclusion of such a field (satisfying $\partial_r \mathcal{B}^r = 0$) does not alter the analytic solution for any of the primitive fields (ρ, P, or u^r), yet it serves as a non-trivial numerical test of the magnetic field terms in the code. The magnitude of the magnetic field is set by $\|B^2\|/(4\pi\rho) = 10.56$ ($\beta \approx 1$) at $r = r_c$. With magnetic fields included, the magnitudes of the errors increase to 3.89×10^{-3} and 1.36×10^{-3} for the AV and eAV methods with 256 zones, but the convergence rates remain the same - 1.3 and 1.4, respectively. We note that the divergence error in the magnetic field does not build up appreciably during the course of these runs - $\sum |\partial_i \mathcal{B}^i| \lesssim 10^{-14}$ in all cases. Since we intend primarily to use either the AV or eAV methods for this type of research application, we have not extended the NOCD algorithm to account for the proper characteristic magnetohydrodynamic speed in arbitrarily curved spacetimes, so we do not report results from that method in this or the following section.

4.2.4. Magnetized Black Hole Torus

Next we consider the astrophysically interesting problem of a magnetized torus of gas orbiting a rotating black hole. Although there is no known analytic solution for this problem, it is sufficiently well documented in the literature to serve as a useful test of the code. It also represents one class of problems for which *Cosmos* $++$ is intended to be used. We set this problem up using the same parameters as model SFP-2D of De Villiers & Hawley (2003b); specifically, the spin of the black hole is $a/M = 0.9$, the specific angular momentum of the torus is $l/M = 4.3$, the surface potential of the torus is $(u_t)_{in} = -0.98$, and the equation of state of the gas is set by the polytropic constant $\kappa = 0.01$ and index $\Gamma = 5/3$. To this torus we add initially weak poloidal magnetic field loops to seed the magneto-rotational instability (MRI, Balbus & Hawley 1991). The initial magnetic field vector potential is (De Villiers & Hawley 2003a)

$$A_\phi = \begin{cases} k(\rho - \rho_{cut}) & \text{for} \quad \rho \geq \rho_{cut} \; , \\ 0 & \text{for} \quad \rho < \rho_{cut} \; . \end{cases} \tag{75}$$

The non-zero spatial magnetic field components are then $\mathcal{B}^r = -\partial_\theta A_\phi$ and $\mathcal{B}^\theta = \partial_r A_\phi$. These poloidal field loops coincide with the isodensity contours of the torus. The parameter $\rho_{cut} = 0.5 * \rho_{max}$ is used to keep the

field a suitable distance inside the surface of the torus. The initial setup of the torus is illustrated in Figure 15(a), which shows a plot of the logarithm of ρ. Using the constant k in equation (75), the field is normalized such that initially $\beta = P/(||B||^2/8\pi) \geq \beta_0 = 2$ throughout the torus. This initialization is slightly different than De Villiers & Hawley (2003b), who use a volume integrated β to set the field strength; the difference is such that $\beta_0 = 100$ in their work is roughly comparable to $\beta_0 = 2$ here.

For these tests, we only consider two-dimensional, axisymmetric simulations using our AV method. In later applications, we will employ the full three-dimensional capability of $Cosmos++$. This simulation uses a logarithmic radial coordinate of the form $\eta = 1 + \ln(r/r_{BH})$ and a concentrated latitude coordinate x_2 of the form $\theta = x_2 + \frac{1}{2}(1-h)\sin(2x_2)$ with $h = 0.5$. The grid covers the angular scale $0.02\pi \leq \theta \leq 0.98\pi$ and has radial boundaries $r_{min} = 0.98r_{BH}$ and $r_{max} = 120M$.

Figure 15 shows the mass density distribution at $t/(GM/c^3) = 0$, 1250, and 2300 (roughly 0, 3, and 6 orbits at the initial pressure maximum). For a more quantitative comparison, Figure 16 shows the time history of the mass accretion rate through the inner radial boundary of the grid. Comparing with Figure 18 of De Villiers & Hawley (2003b), we see similar amplitudes and frequencies of variability in the accretion flow, particularly for the first 4 orbits. We also find a similar value for the total mass accretion: $\Delta M/M_0 = 0.13$ after 6 orbits here versus 0.14 after 10 orbits in De Villiers & Hawley (2003b). The accretion tapers off to a low value after about 3.5 orbits as expected since MRI turbulence cannot be sustained indefinitely in an axisymmetric simulation, due to Cowling's antidynamo theorem. Throughout this simulation the divergence of the magnetic field is held below a tolerable limit ($\sum |\partial_i \mathcal{B}^i| \sim 0.01$) through the use of the divergence cleanser. Importantly, this divergence error does not increase with time.

5. Discussion

We have developed a new object oriented code $Cosmos++$ for solving the fully general relativistic magnetohydrodynamics equations on adaptive, unstructured meshes using discrete finite volume and dimensionally unsplit methods. Three basic numerical schemes have been implemented and tested using both internal and total conservative energy formulations: The first evolves internal energy with artificial viscosity for shock capturing; the second uses a nonoscillatory central difference scheme to solve the fully conservative (energy and momentum) form of equations; and the third approach combines the internal and conservative energy equations with artificial viscosity methods to achieve greater accuracy in highly relativistic regimes.

We find by comparing the different methods presented here with other published results, including Riemann-solver based codes, that, despite their simplicity, artificial viscosity methods perform quite well for low to moderately boosted flows, ($V/c \simeq 0.95$ in the shock tube and wall shock tests). This is consistent with our conclusions from earlier work using dimensionally split, finite difference methods on structured grids (Anninos & Fragile 2003). However, it is well known that for higher velocity flows, traditional AV methods tend to break down. We have demonstrated that the basic AV approach can be extended easily to the ultra-relativistic regime by simply incorporating a dual energy formalism (the eAV method) to solve both internal and conservative energy equations with standard operator split procedures. This eAV procedure results in significantly improved shock and wave capturing capabilities that allows AV schemes to model flows at arbitrarily high boosts. We have presented stable, accurate solutions for strong shock collision interactions with boosts (velocities) easily exceeding 200 (0.99999c).

The NOCD method implemented here, although of a slightly different family of algorithms than we adopted in our previous code, also works quite well in the high boost regime. In fact this method has signif-

icantly less numerical diffusion and is less sensitive to Courant restrictions than our earlier implementation (Anninos & Fragile 2003). The eAV and NOCD methods thus provide robust alternatives to simulating highly relativistic flows since they are comparable in accuracy, over the entire range of velocities we have simulated, to more complicated Riemann-based codes for both hydrodynamic and magnetohydrodynamic problems.

Fig. 4.— Mean relative errors in density for the AV, eAV, and NOCD methods as a function of boost for the relativistic wall shock problem. All calculations were run using 200 zones up to time $t = 2.0$. The AV and eAV results can be improved significantly and brought closer in alignment with the NOCD results by reducing the Courant factor or increasing the viscosity coefficients over the canonical values we have chosen.
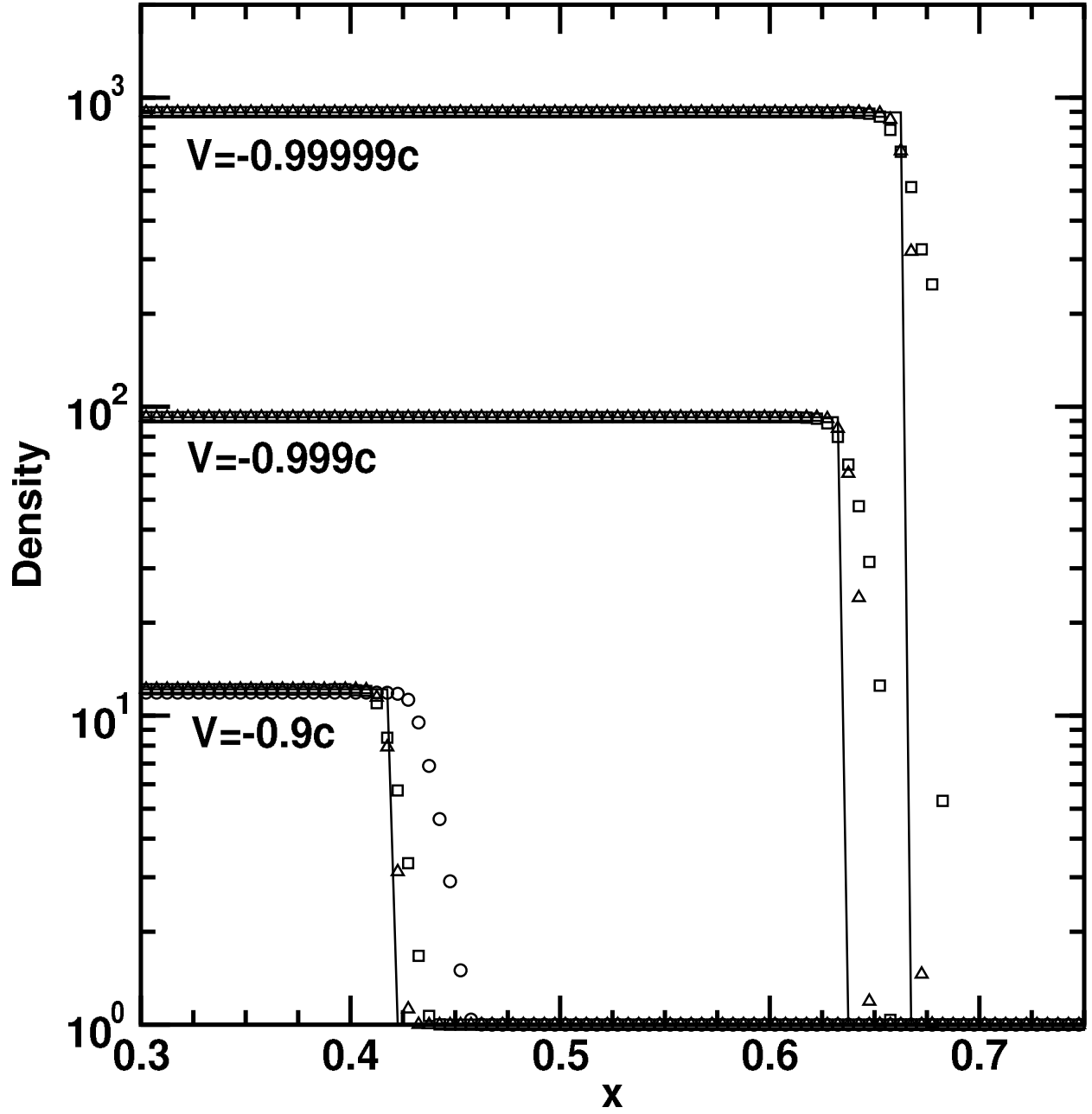
Fig. 5.— Density plots for different infall velocities in the wall shock test using the eAV (*squares*) and NOCD (*triangles*) methods. Results for the AV method (*circles*) are only included for $V = -0.9$. The resolution is 200 zones, the displayed time is $t = 2.0$, and the graphs are zoomed in at the shock fronts to distinguish the different solutions.
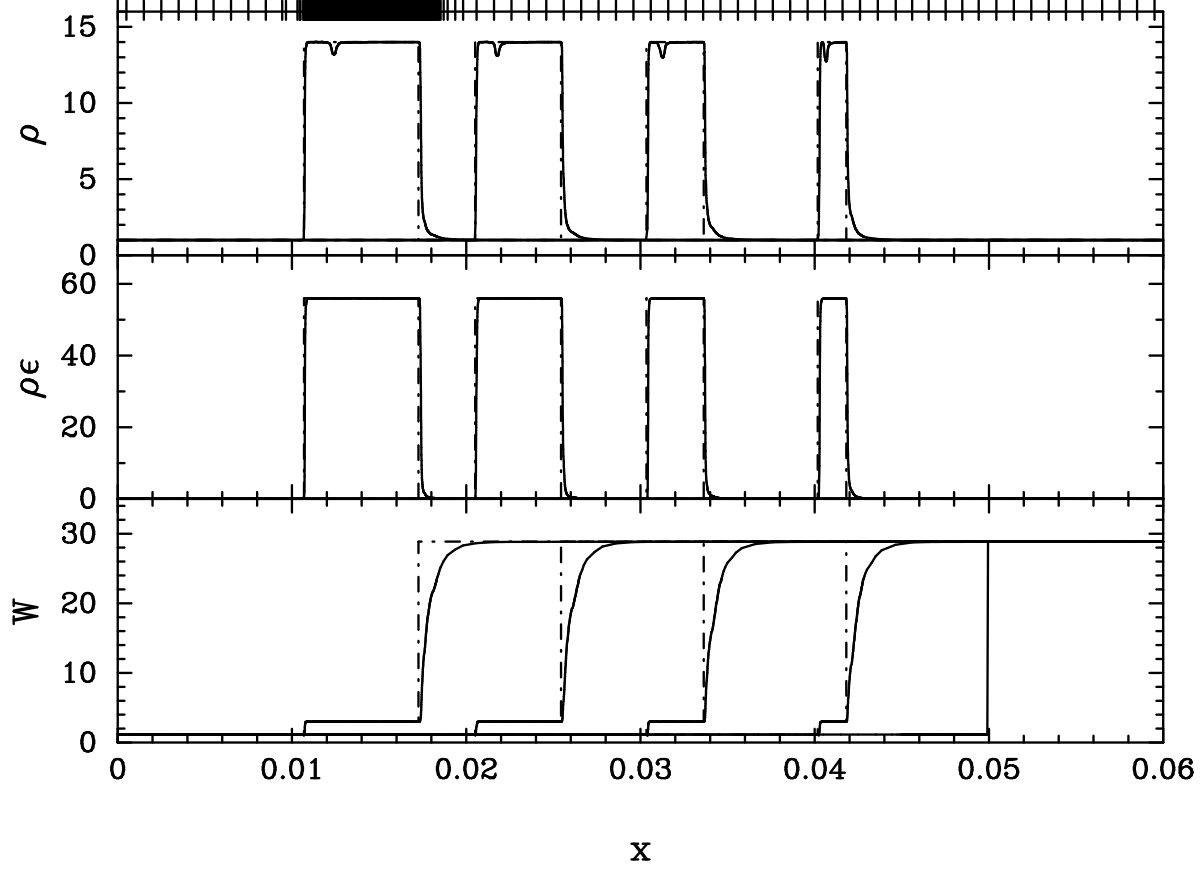
Fig. 6.— Two ideal fluids, each with initial proper density $\rho = 1$, proper energy $\rho\epsilon = 10^{-8}$, and $\Gamma = 5/3$, collide initially at $x = 0.05$. The fluids move in opposite directions, each with $W' = 5$ in the center-of-momentum frame. The observer is boosted to the right at $W = 3$ so the fluid moves at speeds up to $V/c \sim 0.999$, and the shocked fluid region can be seen to move to the left over a sequence of five times, $t = 0.0, 0.01, 0.02, 0.03, 0.04$. The numerical results are solid lines and show good agreement with the analytical solution (Table 2) shown in dot-dashed lines. The ticks at the top of the plot are zone positions for the last time snapshot. This problem uses a base resolution of 60 zones, with eight allowed levels of mesh refinement.
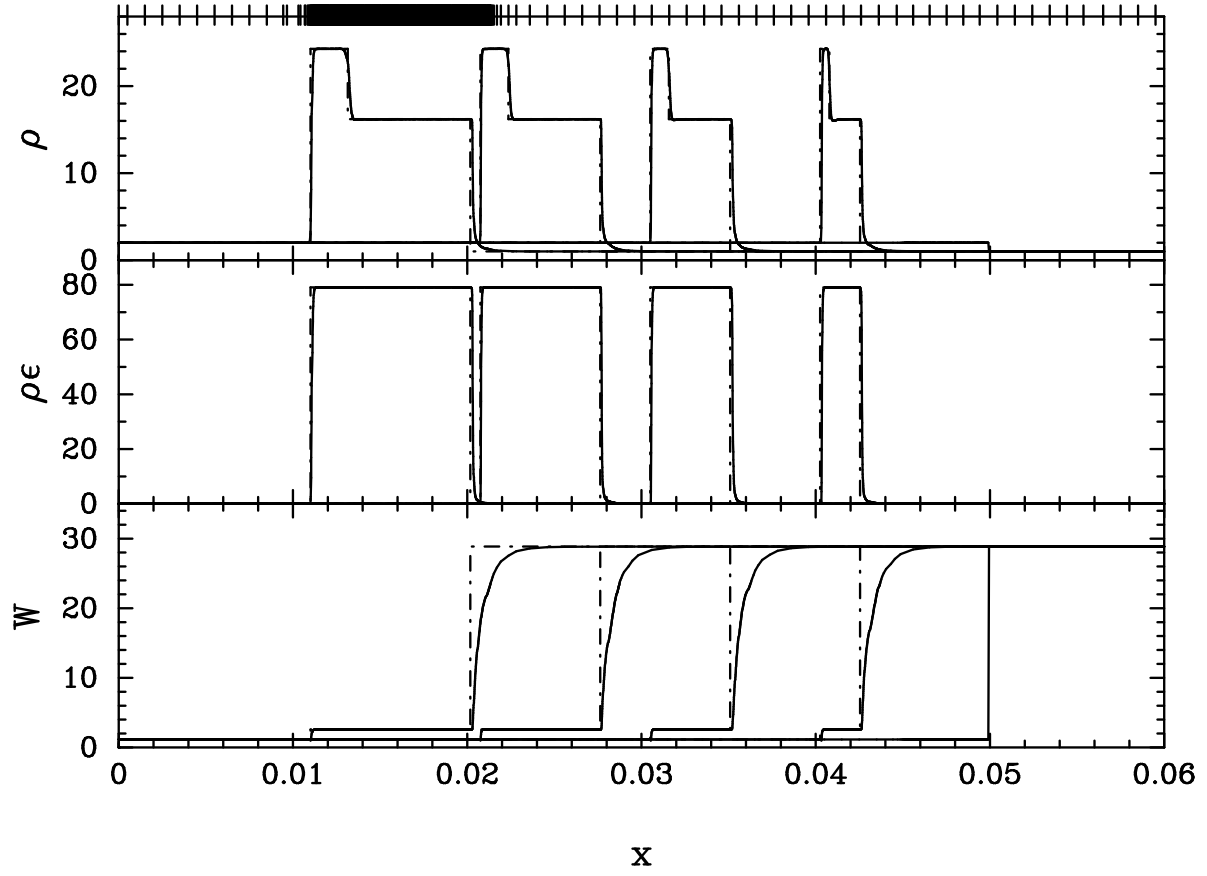
Fig. 7.— As in Figure 6 except the two ideal fluids have unmatched initial proper densities $\rho_1 = 2$, $\rho_2 = 1$.
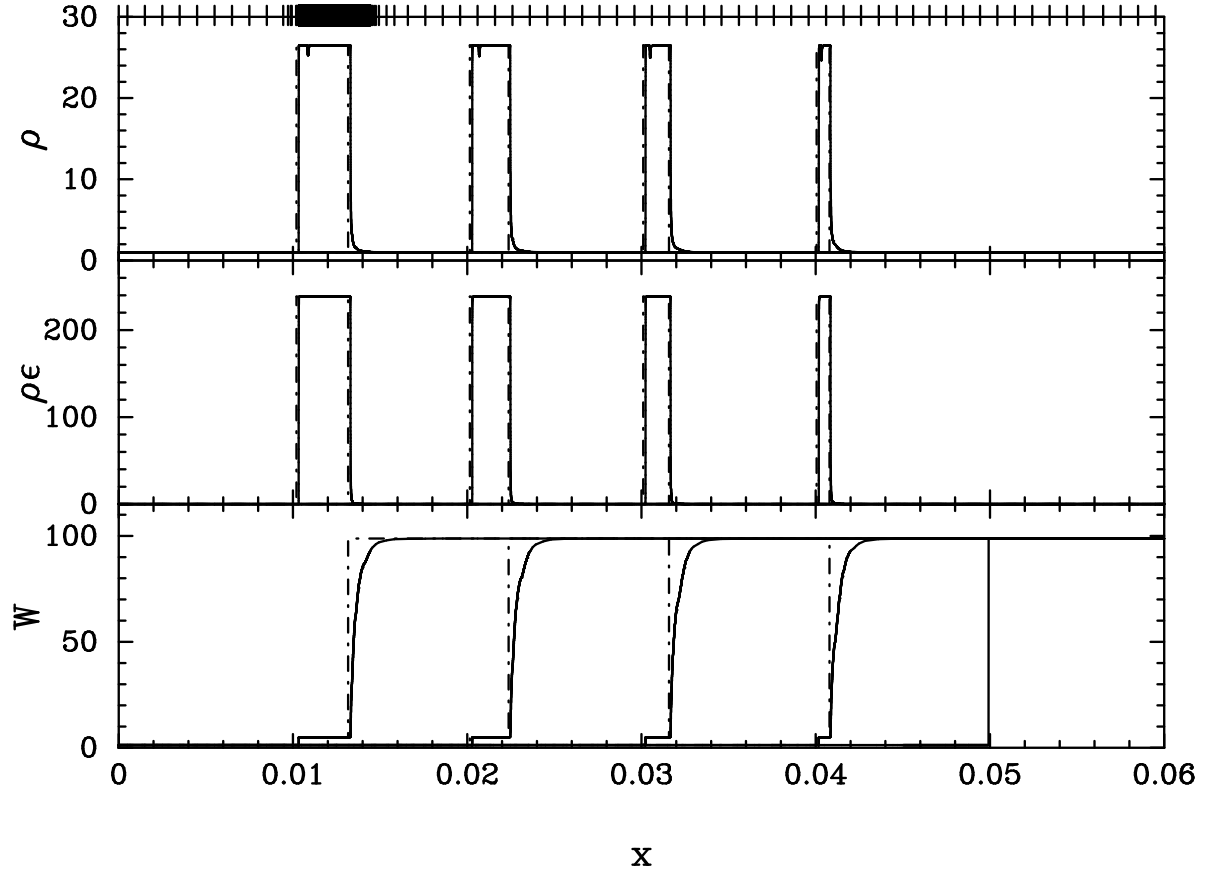
Fig. 8.— As in Figure 6 except here $W' = 10$ and the observer is boosted to the right at $W = 5$. The base resolution is 60 zones and 12 levels of mesh refinement are allowed.
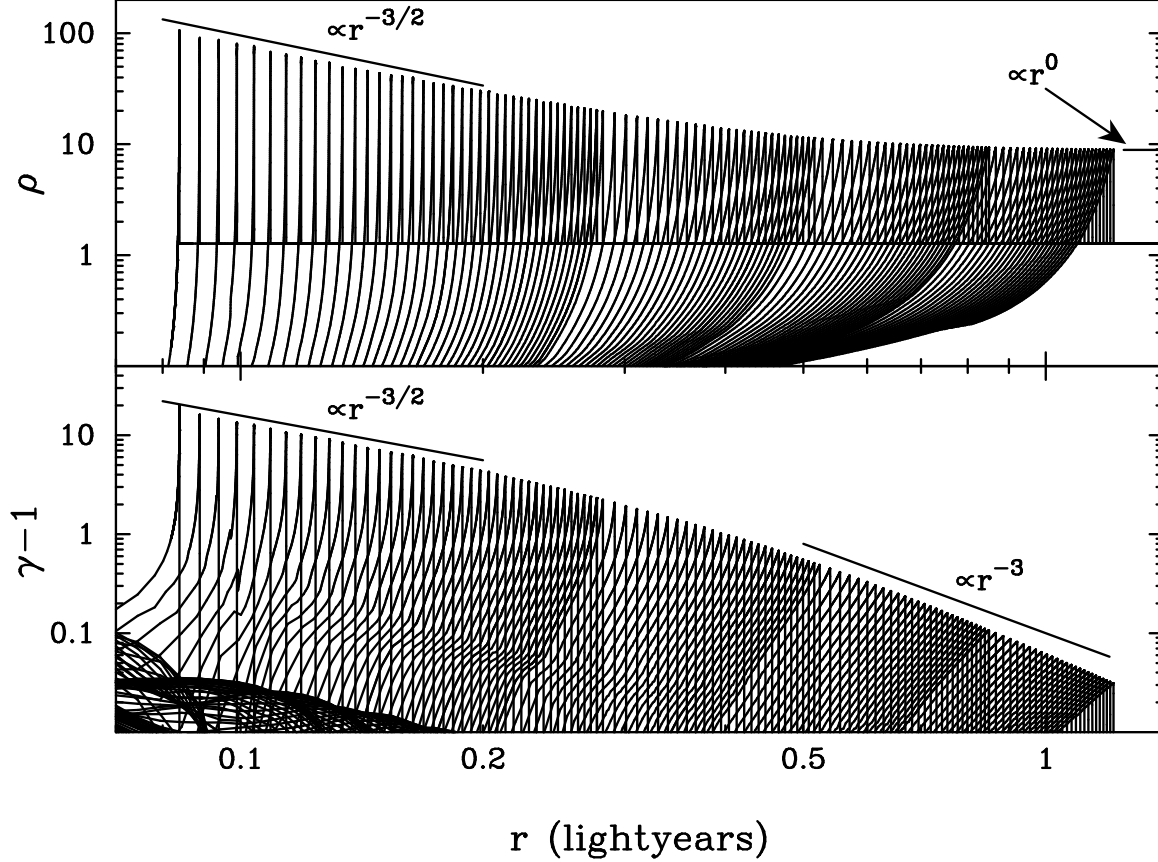
Fig. 9.— A spherical relativistic blastwave with energy $E_{\mathrm{BM}} = 1$ foe $\equiv 10^{51}$ ergs, $\gamma_{\mathrm{BM}} = 30$, plows into an external density of $\rho_{\mathrm{BM}} = 1$ baryon cm$^{-3} = 1.27$ foe lightyear^{-3} from an initial radius $r_{\mathrm{BM}} = 0.084$ lightyear. The material immediately behind the shock is initially shocked to $\rho = 2^{3/2} \gamma_{\mathrm{BM}} \rho_{\mathrm{BM}}$, $\gamma = \gamma_{\mathrm{BM}}/\sqrt{2}$ and evolves as $\rho \propto \gamma - 1 \propto r^{-3/2}$. Once the blastwave decelerates to $\gamma \sim 1$ it transitions to the non-relativistic Sedov-Taylor blastwave for which the shocked material evolves as $\rho = \rho_{\mathrm{BM}} (\Gamma + 1)/(\Gamma - 1) = 8.9$ foe lightyear^{-3}, $\Gamma = 4/3$, and $\gamma - 1 \propto v^2 \propto r^{-3}$ (Landau & Lifshitz 1959). This simulation uses the NOCD method. For this figure the dump frequency was halved periodically to allow late time profiles to be resolved.
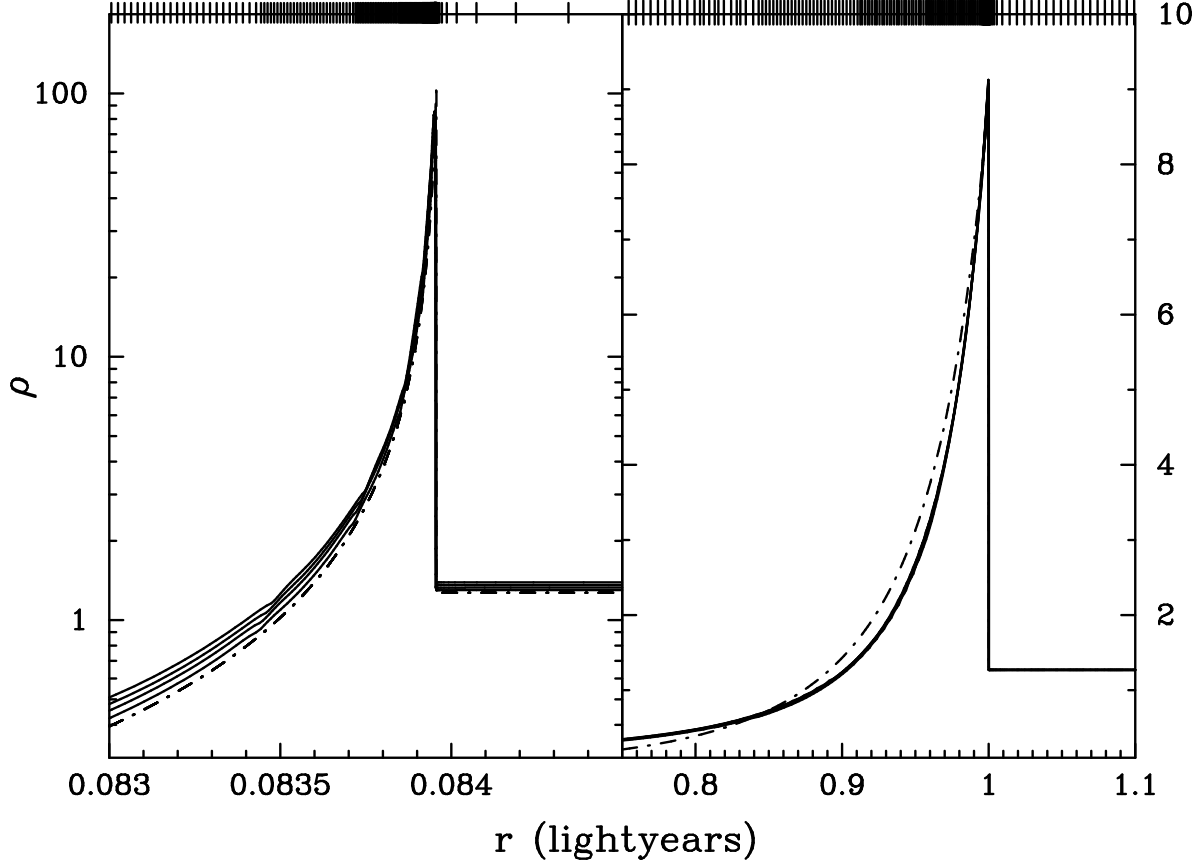
Fig. 10.— Self-similarity of the relativistic (left) and non-relativistic (right) phases of the blastwave of Figure 9. As discussed in the text, the relativistic (left) panel demonstrates the eAV method, while the non-relativistic (right) panel uses the NOCD method. At left, the initial relativistic proper density profile, $\rho = D/W$, (dot-dashed line) of eqn. (66) is plotted with four subsequent profiles at $\sim 100,000$ cycle intervals. Each profile is scaled in radius to align with the initial shock front and the density is scaled by $\rho \propto r^{-3/2}$. Save an initial decrease in the magnitude of the peak of about 10%, and a gradual increase in the density of the lower velocity tail, the self-similar profile is well maintained. At right, the Sedov solution (dot-dashed line, e.g. Landau & Lifshitz 1959) with $\Gamma = 4/3$ is plotted with six density profiles from the non-relativistic phase of the run from Figure 9. The radii, ranging from 1 to 1.2 lightyears for times 1.33 to 2 years respectively, are scaled to the radius of one lightyear. The shocked density $\rho = \rho_{BM}(\Gamma + 1)/(\Gamma - 1) = 8.9$ foe lightyear^{-3} is not scaled, but is naturally captured by the code to within a few percent. The scaled profiles are virtually identical to each other and well reproduce the Sedov profile. Tick marks at the top of the plots show the mesh nodes for a typical profile. The left (right) plot has 17 (8) allowed levels of refinement.
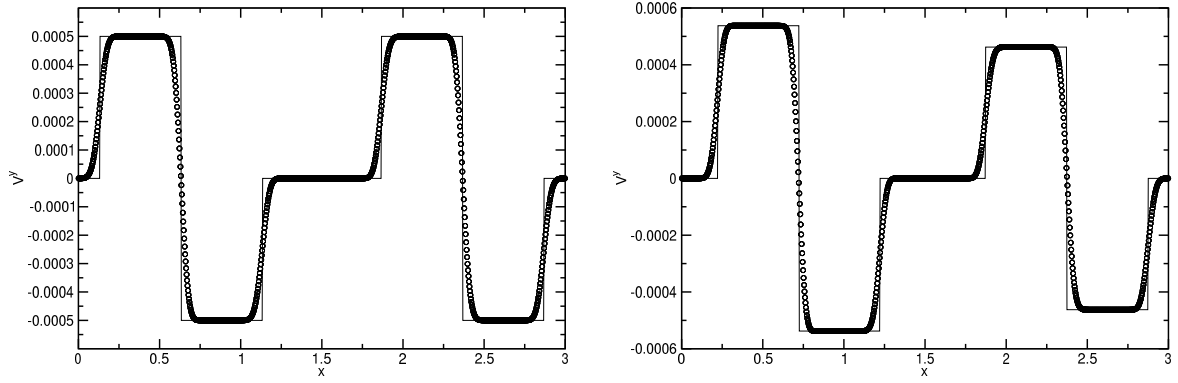
Fig. 11.— Tranverse velocity V^y for two cases of the Alfvén wave test: (a) case A at $t = 0.9$ and (b) case B at $t = 1.1$. The numerical resolution is 1024 zones; the solid lines are the analytic solutions.
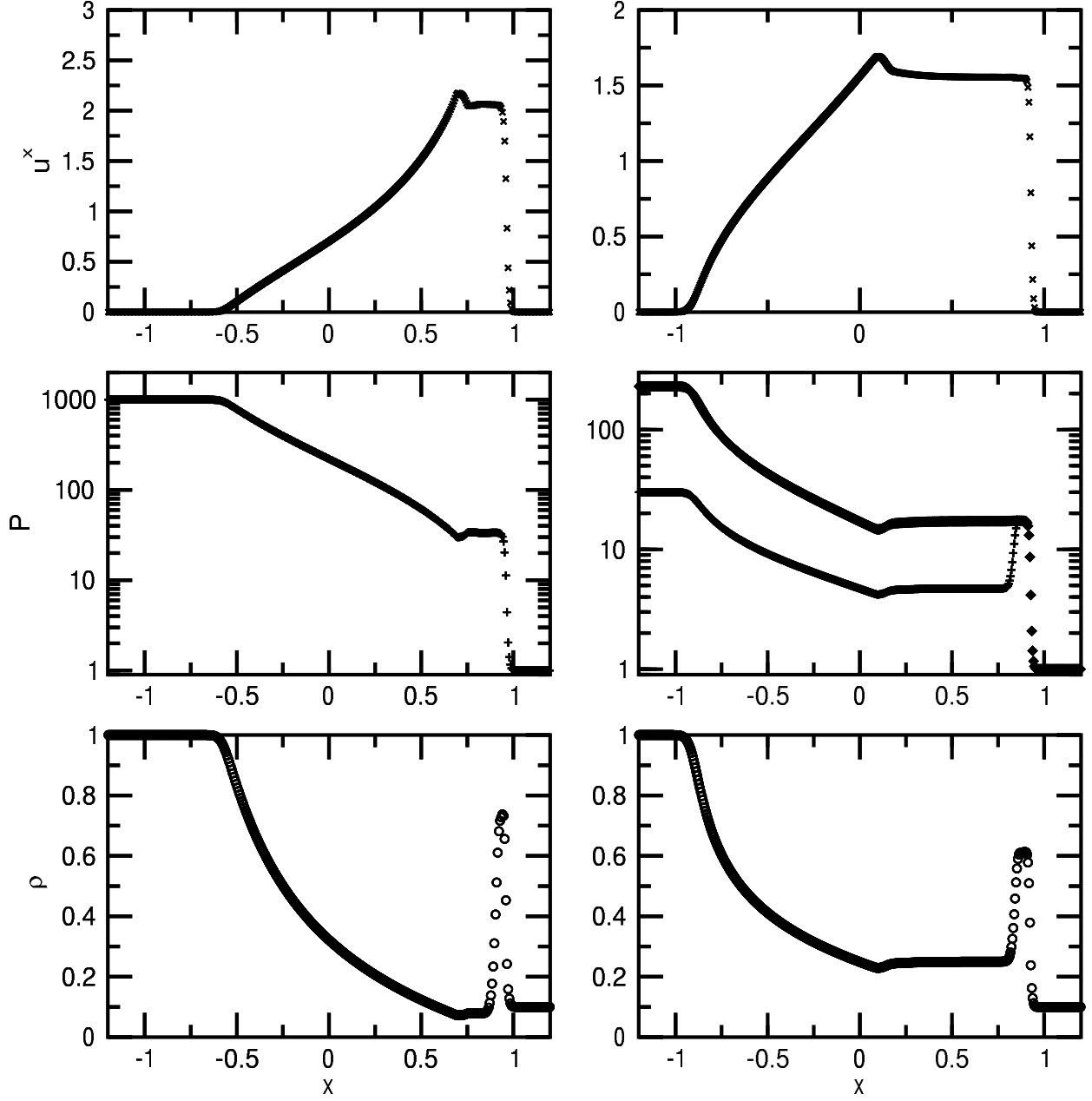
Fig. 12.— *Left panel:* Magnetosonic shock tube problem 1 from Komissarov (1999). The magnetic field is normal to the initial discontinuity (at $x = 0$) so it does not play a dynamical role. The symbols show the numerical solution at $t = 1$ for 400 zones using the AV method. *Right panel:* Magnetosonic shock tube problem 2 from Komissarov (1999). The initial magnetic field to the left of $x = 0$ is parallel to the discontinuity, while the field is absent to the right. The symbols show the numerical solution at $t = 1$ for 500 zones using the AV method.
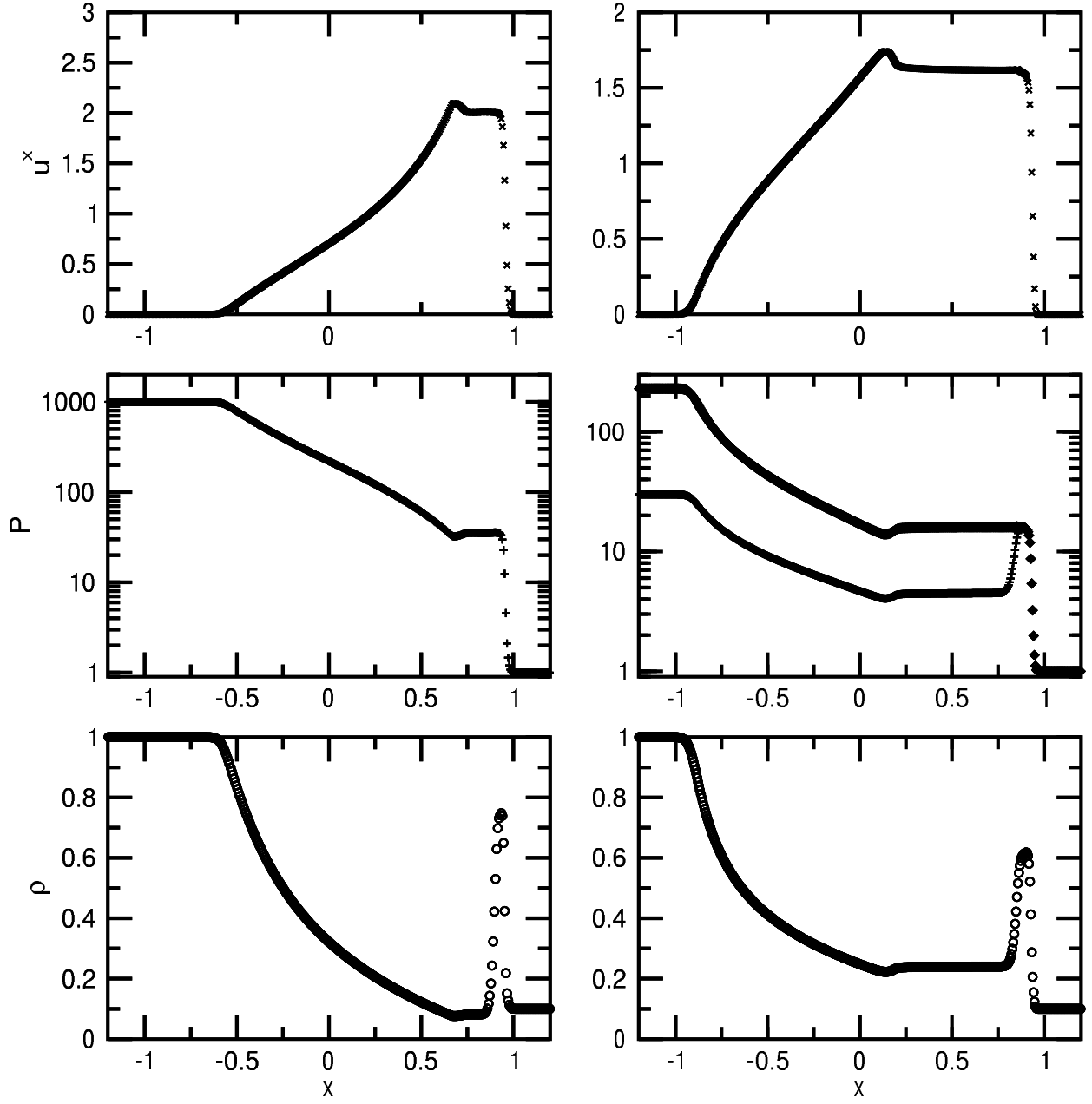
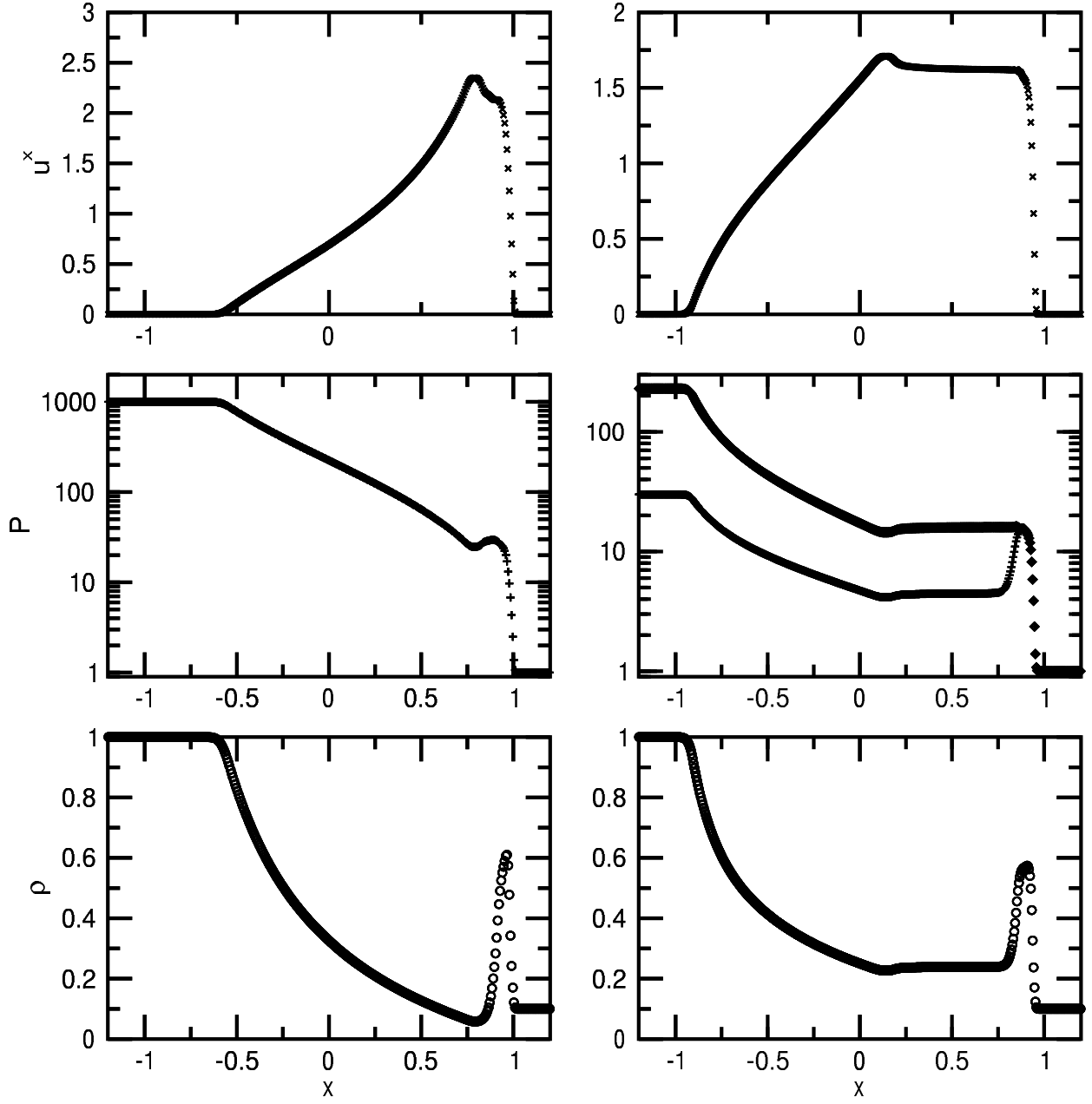Fig. 13.— As Figure 12 but with the extended viscosity (eAV) scheme.

Fig. 14.— As Figure 12 but with the non-oscillatory central difference (NOCD) scheme.
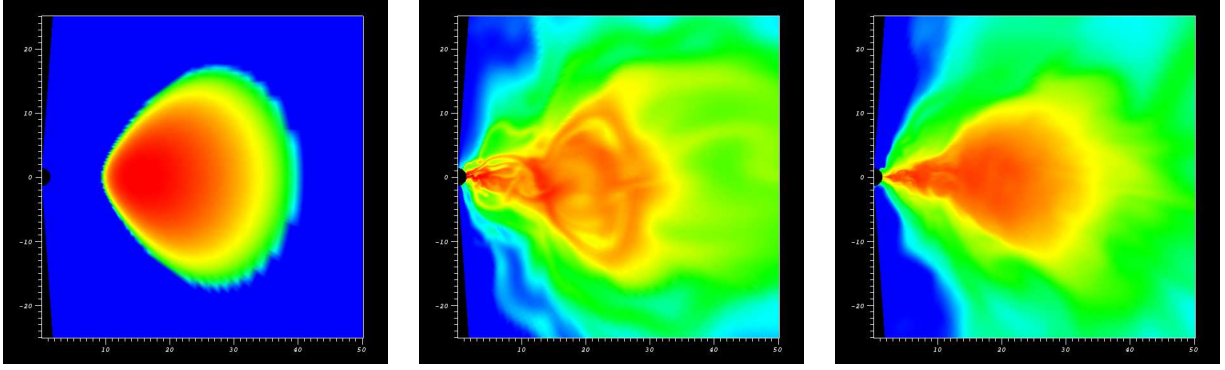
Fig. 15.— Plot of gas density ρ at (a) $t = 0$, (b) $t = 1250M = 3\tau_{orb}$, and (c) $t = 2300M = 6\tau_{orb}$ for the Kerr-Schild form of the metric. The density is scaled logarithmically over 4 orders of magnitude and maintains the same scale in all three panels.
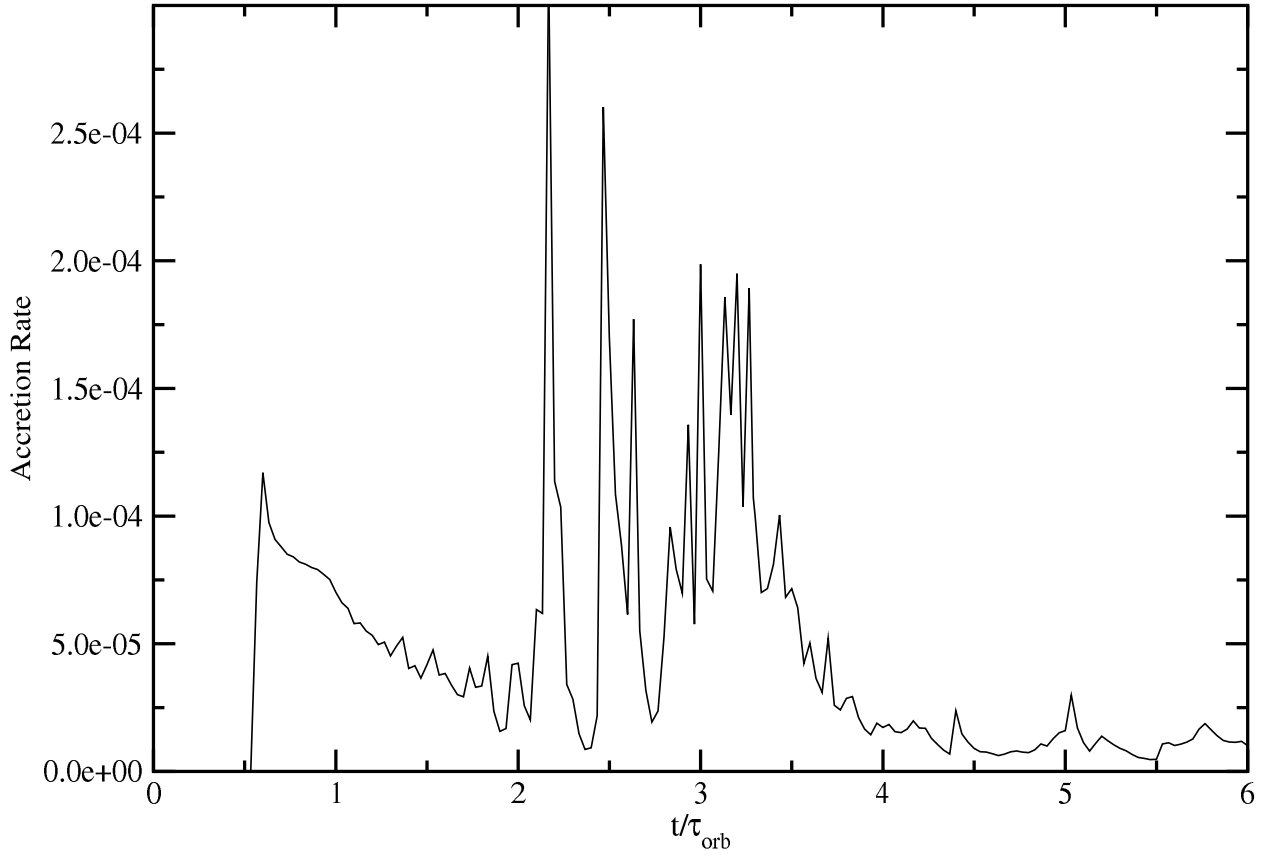

Fig. 16.— Mass accretion rate $\dot{M}$ at the inner radial boundary r_{min} normalized by the initial mass of the torus.

REFERENCES

Anninos, P., & Fragile, P. C. 2003, ApJS, 144, 243

Anninos, P., Fragile, P. C., & Murray, S. D. 2003, ApJS, 147, 177

Balbus, S. A., & Hawley, J. F. 1991, ApJ, 376, 214

Berger, M. J., & Colella, P. 1989, J. Comp. Phys., 82, 64

Berger, M. J., & Oliger, J. 1984, J. Comp. Phys., 53, 484

Blandford, R. D., & McKee, C. F. 1976, Phys.Fluids, 19, 1130

De Villiers, J., & Hawley, J. F. 2003a, ApJ, 589, 458

De Villiers, J., & Hawley, J. F. 2003b, ApJ, 592, 1060

Font, J. A., Ibáñez, J. M. ., & Papadopoulos, P. 1998, ApJ, 507, L67

Fragile, P. C., & Anninos, P. 2003, Phys. Rev. D, 67, 103010

Fragile, P. C., & Anninos, P. 2005, ApJ, 623, 347

Fragile, P. C., Anninos, P., Gustafson, K., & Murray, S. D. 2005, ApJ, 619, 327

Gammie, C. F., McKinney, J. C., & Tóth, G. 2003, ApJ, 589, 444

Hawley, J. F., Smarr, L. L., & Wilson, J. R. 1984, ApJS, 55, 211

Hawley, J. F., Wilson, J. R., & Smarr, L. L. 1984, ApJ, 277, 296

Khokhlov, A. M. 1998, J. Comp. Phys., 143, 519

Koide, S., Shibata, K., & Kudoh, T. 1999, ApJ, 522, 727

Komissarov, S. S. 1999, MNRAS, 303, 343

Kurganov, A., & Tadmor, E. 2000, J. Comp. Phys., 160, 241

Landau, L. D., & Lifshitz, E. M. 1959, Fluid Mechanics, Course of theoretical physics, Oxford: Pergamon Press, 1959

Michel, F. C. 1972, Ap&SS, 15, 153

Papadopoulos, P., & Font, J. A. 1998, Phys. Rev. D, 58, 24005

Shu, C. W., & Osher, S. 1988, J. Comp. Phys., 77, 439

Stone, J. M., Hawley, J. F., Evans, C. R., & Norman, M. L. 1992, ApJ, 388, 415

Tscharnuter, W. M., & Winkler, K. H. 1979, Comput. Phys. Comm., 18, 171

von Neumann, J., & Richtmyer, R. D. 1950, J. Appl. Phys., 21, 232

White, J. W. 1973, J. Comp. Phys., 11, 573

Wilson, J. R. 1972, ApJ, 173, 431

Wilson, J. R. 1979, in Sources of Gravitational Radiation, 423

Grid	Method	$\|E(\rho)\|_1$	$\|E(P)\|_1$	$\|E(V)\|_1$
400	AV	1.24×10^{-1}	2.78×10^{0}	1.38×10^{-2}
	eAV	1.82×10^{-1}	4.23×10^{0}	1.99×10^{-2}
	NOCD	1.69×10^{-1}	3.98×10^{0}	2.00×10^{-2}
800	AV	8.09×10^{-2}	1.61×10^{0}	7.78×10^{-3}
	eAV	9.00×10^{-2}	2.06×10^{0}	1.04×10^{-2}
	NOCD	1.04×10^{-1}	2.00×10^{0}	1.08×10^{-2}
1600	AV	5.03×10^{-2}	1.01×10^{0}	4.41×10^{-3}
	eAV	5.18×10^{-2}	1.01×10^{0}	5.24×10^{-3}
	NOCD	6.59×10^{-2}	1.02×10^{0}	5.80×10^{-3}
3200	AV	3.83×10^{-2}	7.12×10^{-1}	2.35×10^{-3}
	eAV	2.46×10^{-2}	4.85×10^{-1}	2.29×10^{-3}
	NOCD	3.14×10^{-2}	5.17×10^{-1}	2.71×10^{-3}

Table 1: L-1 Norm errors in density, pressure, and velocity for the hydrodynamic shock-tube test at time $t = 0.36$. Convergence is approximately linear as expected for problems with shock discontinuities.

ρ_1	W_1	W_r	ρ_2	W_d	e_d	ρ_3	W_f	ρ_4	W_4
1.0	1.1436	5.412	14.0	3.0	56.0	14.0	1.741	1.0	28.86
2.0	1.1436	4.482	24.28	2.572	79.06	16.20	1.500	1.0	28.86
1.0	1.2558	9.973	26.5	5.0	238.5	26.5	2.565	1.0	98.74

Table 2: Analytical results for boosted collisions shown in Figs 6, 7 & 8 (see §4.1.3). Initial conditions are given by ρ_1, W_1, ρ_4, W_4. W_d is solved for by Equations (54) & (61) in the center-of-momentum frame, and then boosted into the lab frame. Shocked proper densities ρ_2 and ρ_3 are given by eqns. (56), and the proper energy density of the contact discontinuity is $e_d = \epsilon_2\rho_2 = \epsilon_3\rho_3$ with eqns. (58). The boosts of the reverse and forward shock fronts, W_r and W_f, are calculated from their center-of-momentum velocities (eqn. (60)).